



Measuring short-term post-fire forest recovery across a burn severity gradient in a mixed pine-oak forest using multi-sensor remote sensing techniques

Ran Meng^{a,*}, Jin Wu^a, Feng Zhao^b, Bruce D. Cook^c, Ryan P. Hanavan^d, Shawn P. Serbin^a

^a Environmental & Climate Sciences Department, Brookhaven National Laboratory, Upton, New York, NY 11973, USA

^b Department of Geographical Sciences, University of Maryland, 1165 Lefrak Hall, College Park, MD 20742, USA

^c Biospheric Sciences Branch, NASA Goddard Space Flight Center, Greenbelt, MD 20742, USA

^d USDA Forest Service, Northeastern Area State & Private Forestry, 271 Mast Rd., Durham, NH 03824, USA

ARTICLE INFO

Keywords:

Burn severity
Species-specific post-fire responses
Fire adaptive strategies
WorldView-2
Vegetation classification
Hyperspectral data
Forest composition and structure

ABSTRACT

Understanding post-fire forest recovery is pivotal to the study of forest dynamics and global carbon cycle. Field-based studies indicated a convex response of forest recovery rate to burn severity at the individual tree level, related with fire-induced tree mortality; however, these findings were constrained in spatial/temporal extents, while not detectable by traditional optical remote sensing studies, largely attributing to the contaminated effect from understory recovery. Here, we examined whether the combined use of multi-sensor remote sensing techniques (i.e., 1 m simultaneous airborne imaging spectroscopy and LiDAR and 2 m satellite multi-spectral imagery) to separate canopy recovery from understory recovery would enable to quantify post-fire forest recovery rate spanning a large gradient in burn severity over large-scales. Our study was conducted in a mixed pine-oak forest in Long Island, NY, three years after a top-killing fire. Our studies remotely detected an initial increase and then decline of forest recovery rate to burn severity across the burned area, with a maximum canopy area-based recovery rate of 10% per year at moderate forest burn severity class. More intriguingly, such remotely detected convex relationships also held at species level, with pine trees being more resilient to high burn severity and having a higher maximum recovery rate (12% per year) than oak trees (4% per year). These results are one of the first quantitative evidences showing the effects of fire adaptive strategies on post-fire forest recovery, derived from relatively large spatial-temporal scales. Our study thus provides the methodological advance to link multi-sensor remote sensing techniques to monitor forest dynamics in a spatially explicit manner over large-scales, with important implications for fire-related forest management and constraining/benchmarking fire effect schemes in ecological process models.

1. Introduction

Global fire emissions are an annual carbon flux of around 2.1 Pg C per year, equivalent to 50%–200% of annual terrestrial carbon sink (Piao et al., 2009; van der Werf et al., 2009; van der Werf et al., 2010). Among these fire emissions, 35% are forest-related (van der Werf et al., 2009; van der Werf et al., 2010). Post-fire forest recovery, a successional process towards the pre-fire structure and function, or to an alternative state, can lead to a significant carbon sink, generating offsets to the large fire-induced carbon losses (Amiro et al., 2003; Hicke et al., 2003; Turner et al., 2016). Such post-fire forest recovery is tightly connected to burn severity, a metric of fire effects on forest composition and structure, showing strong spatial heterogeneity across the

landscape (Bolton et al., 2015; Jin et al., 2012; Morgan et al., 2014; Turner et al., 1997). Understanding how forests recover from disturbances such as fire, especially the quantitative relationship between forest recovery rate and burn severity, has long been a central focus for forest ecology and global carbon cycle studies, and is becoming a pressing issue for global change biologists, particularly with increasing frequencies and intensities of fire disturbances under the projected drier and warmer future climate (Bowman et al., 2009; Dale et al., 2001; Harvey et al., 2014; Meng et al., 2015; Turner, 2010; Westerling et al., 2006; Yang et al., 2015; Yang et al., 2017).

Separating post-fire forest canopy recovery from understory recovery is scientifically important, having broad implications for forest management (Castro et al., 2011; Kotliar et al., 2002), understanding

* Corresponding author.

E-mail address: ranmeng@bnl.gov (R. Meng).

fire effects on the terrestrial water cycle (Lewis et al., 2006; Mayor et al., 2007), and for simulating the global carbon cycle in Earth System Models (Fisher et al., 2015; Fisher et al., 2017). Specifically, understory (e.g., shrub, herbaceous, and woody) vegetation can recover quickly after the fire even with high burn severity (Figs. S1 & S2), however this vegetation is not the same, functionally and structurally, as the pre-fire canopy, having large differences in lifeform, productivity and capacity for carbon and water storage (Little and Moore, 1949; Swanson et al., 2011). Thus here we refer post-fire forest recovery to the increase in tree canopy areas during the post-fire period. As we focus on quantifications of post-fire tree canopy area recovery in this study, we define burn severity as the extent of tree canopy area loss by fire following previous studies (Meng et al., 2017; Quintano et al., 2013).

Several previous field-based studies have been conducted to explore the relationship between burn severity and short-term (< 5 years) post-fire forest responses (Balch et al., 2011; Brando et al., 2012; Smith et al., 2016; Sparks et al., 2016). Short-term post-fire recovery is critical for the long-term forest regeneration and can provide important insights about forest dynamics (Mantgem et al., 2006; Meng et al., 2015; Swanson et al., 2011). Although these field-based studies are primarily experiment-based, focusing on the threshold of burn severity in tree mortality at individual tree or coarse stand-scale not directly post-fire forest recovery, their results indicate trees or seedlings canopy areas can recover most from intermediate burn severity before reaching the threshold of burn severity in tree mortality (Brando et al., 2012; Sparks et al., 2016). These results are consistent with forest recovery studies in twenty-four years after the Greater Yellowstone fire with high resolution satellite imagery (see Fig. 8 in Zhao et al., 2016). Additionally, these experiment-based fire studies provide comparable results to other field-based studies examining various other disturbance drivers (e.g., herbivory, drought, and hurricane), also finding that forests recover most under intermediate disturbance impacts during the short-term period, with no or little forest recovery rate under very high disturbance extent (Hoogesteger and Karlsson, 1992; Lloret et al., 2004; Rich et al., 2007). These field-based studies thus collectively suggest that there exist convex relationships between post-disturbance forest recovery rate and disturbance severity during the short-term period (Fig. 1a).

In spite of the community canopy level relationship between forest recovery rate and burn severity, previous field-based studies suggest that the post-fire forest response can also vary across species (Bond and Keeley, 2005; Franklin et al., 2006; Jordan et al., 2003; e.g., Fig. 1a). Such variations in post-fire responses most likely arise from species-specific fire adaptive strategies (Keeley et al., 2011; Pausas and Keeley, 2014). For example, in a mixed pine-oak forest, the dominant pine has thick fire-resilient bark with the ability to recover from crown regrowth or epicormic resprouting; oak stems are more vulnerable to burn heat but can have vigorous sprouts from the root collars (Jordan et al., 2003; Little, 1998). Although these field-based studies shed important insights as to the post-fire recovery process, these studies are laborious, time-consuming, and often only cover small areas given the time and expense of making the observations, and thus are constrained to very limited spatial and temporal extents. Moreover, disturbances often happen in remote regions (e.g., Meng et al., 2015; Serbin et al., 2013) and as such can be difficult to reach for in-situ measurements.

Remote sensing can provide an efficient way for forest fire-related studies over large spatial and temporal scales, and importantly in remote areas (Lentile et al., 2006; White et al., 1996; Zhao et al., 2016). Many studies have used remote sensing measurements to examine how ecosystem-scale post-fire forests recover from different burn severity across a range of biomes, including Boreal (e.g., Goetz et al., 2006; Jin et al., 2012; Serbin et al., 2013), Mediterranean (e.g., Meng et al., 2015; Storey et al., 2016), and Tropical (e.g., Wilson et al., 2015). These previous remote sensing studies primarily relied on using broadband spectral features within the red, near-infrared (NIR), and shortwave near-infrared (SWIR) regions, typically employing spectral vegetation

indices (SVIs), such as the Normalized Difference Vegetation Index (NDVI) at medium to coarse spatial scales (i.e., 15 m to 1 km), to track post-fire vegetation recovery (e.g., Epting and Verbyla, 2005; Goetz et al., 2006; Lee and Chow, 2015; Storey et al., 2016). However, SVIs such as NDVI can saturate at a relatively low leaf area index (Myneni et al., 1997) and the observed signal in medium to coarse resolution satellite imagery can be influenced by the rapid understory recovery leading to a misinterpretation of the recovery patterns (e.g., Figs. S1 & S2; Meng et al., 2015; Serbin et al., 2013), and as such cannot sufficiently separate post-fire canopy from understory recovery (Bolton et al., 2015; Serbin et al., 2013; Meng et al., 2015). This results in an incorrect or apparent recovery trend suggesting a positive increasing recovery rate with burn severity (Fig. 1b) that is not matched in field observations (Fig. 1a, Figs. S1 & S2). In particular, very high burn severity fires create large canopy gaps and enhance light availability for understory, facilitating rapid understory growth (Serbin et al., 2013; Bartels et al., 2016). As such, traditional SVIs-based methods tended to overestimate the short-term post-fire forest recovery rate, especially at high burn severity (Meng et al., 2015; Fig. S2), and can lead to an unrealistic relationship between burn severity and post-fire forest recovery rate (Fig. 1b). Additionally, such remote sensing-based studies are often constrained in their spatial resolution (≥ 30 m) to characterize the patchy post-fire landscapes with strong spatial heterogeneity, as post-fire forest structural characteristics and the fire-induced ecological responses often vary at very high spatial resolution (VHR, i.e., < 5 m) (Alonzo et al., 2017; Meng et al., 2017). Thus these studies cannot meet the increasing demand for conducting operational forest management and studying species-specific post-fire forest responses (Kolden et al., 2012; Meng et al., 2017).

The use of multi-sensor remote sensing observations together could provide new and unique opportunities to help bridge these knowledge gaps (Asner et al., 2017; Cook et al., 2013; Meng et al., 2017). For example, sub-orbital (i.e., airborne) remote sensing platforms, leveraging imaging spectroscopy (IS, i.e., passive high-spectral-resolution of “hyperspectral” reflectance) and Light Detection and Ranging (LiDAR, i.e., active ranging measurements to derive canopy heights and structure), enables the simultaneous measurements of forest optical and structural properties at VHR, by which we expect it can help to separate post-fire forest recovery from understory recovery. For example, several recent studies have demonstrated that the combined use of optical and LiDAR remote sensing measurements allows for more accurate species differentiation (Fassnacht et al., 2016). In addition, the increasing availability of VHR satellite data is enabling forest burn severity mapping at much finer spatial scales than previously available, showing improved performances over traditional 30 m Landsat-based methods (Holden et al., 2010; Meng et al., 2017; Mitri and Gitas, 2008). As such, we expect these multi-sensor remote-sensing techniques to facilitate improved quantifications of the species-specific relationships between forest recovery rate and burn severity (Fig. 1c) from the individual tree scale to the landscape as a whole.

The goal of our work was to explore the combined use of these multi-sensor remote sensing techniques to facilitate species-specific short-term forest recovery rate across a burn severity gradient in a spatially explicit manner. We addressed two specific questions: 1) Will the combined use of multi-sensor remote sensing techniques (to minimize the contaminated effect from understory dynamics) be able to extract the convex relationship between post-fire forest recovery rate and burn severity (Fig. 1c) during the short-term post-fire period as expected from field-based studies (Fig. 1a)? 2) Will our novel remote sensing approach allow for the detection of species-specific post-fire forest responses to different levels of burn severity (i.e., oak vs. pine in our study)?

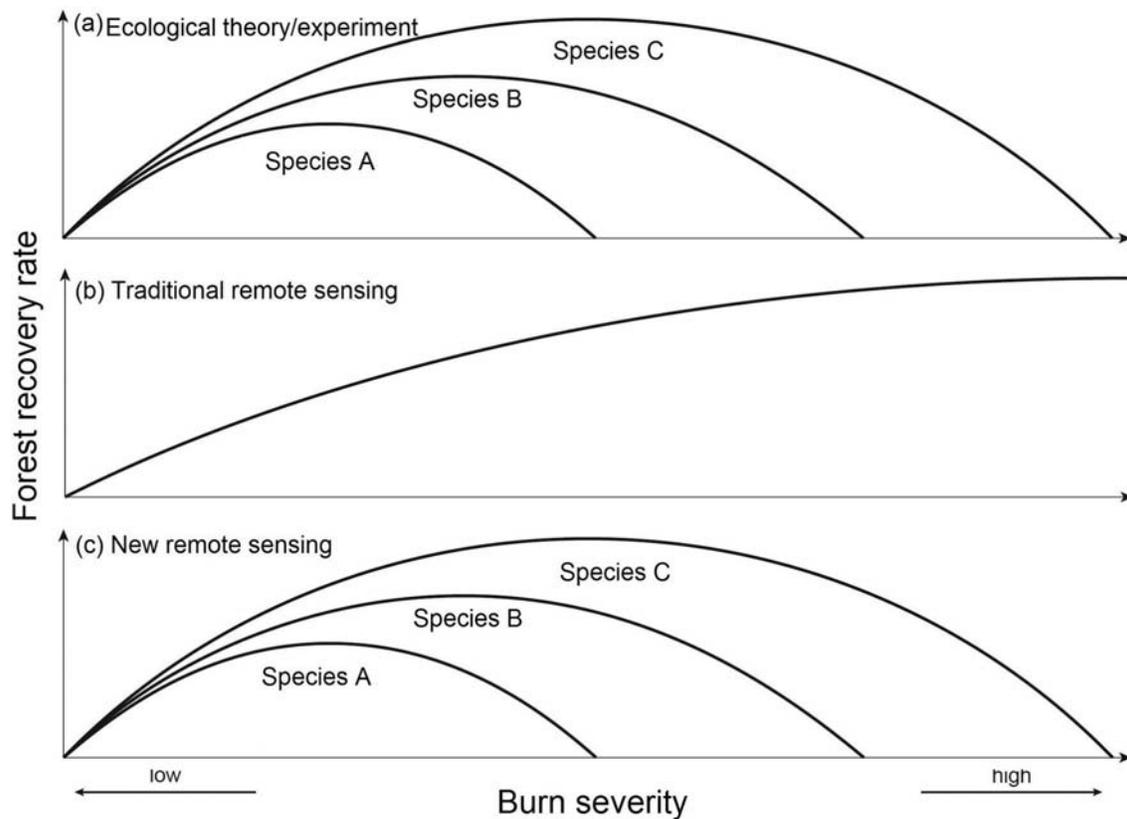


Fig. 1. Three conceptual models showing the relationships of burn severity and forest recovery rate 3–5 year after the fire: (a) Ecological theory/experiment based model (i.e., field experiment at individual tree or coarse stand-scale); (b) Traditional remote sensing based model (i.e., spectral vegetation indices at coarse-moderate spatial resolution (≥ 30 m)); (c) Our proposed new remote sensing based model (i.e., combined use of passive optical and active LiDAR measurement at very high spatial resolution (< 5 m)). Some other factors, such as soil, topography, and post-fire climate, can also affect post-fire forest recovery rate (e.g., Meng et al., 2015; Zhao et al., 2016), but beyond the scope of this study and thus not shown here.

2. Materials

2.1. Study area

The Crescent Bow wildfire broke out in the Central Pine Barrens in Long Island, NY on April 9, 2012 (Fig. 2). Official statistics indicate that > 400 ha areas were burned. The Central Pine Barrens in Long Island, New York was one of largest Pine Barrens areas in United States in history (Jordan et al., 2003; Kurczewski and Boyle, 2000). Pine Barrens are a fire-dependent ecosystem, dominant by pitch pine (*Pinus rigida*) and mixed with other oak species (e.g., white oak (*Quercus alba* L.) and scarlet oak (*Quercus coccinea*)) (Jordan et al., 2003; Kurczewski and Boyle, 2000). As one of its key fire adaptive strategies, pitch pine demonstrates epicormics resprouting, allowing relatively rapid post-fire forest recovery (Pausas and Keeley, 2017), which is different from other fire-adapted pine species relying regeneration from seedbanks (e.g., Lodgepole Pine or Jack Pine) (Sharpe et al., 2017; Zhao et al., 2016). The study area is characterized by sandy soils, relatively flat terrain, and a moderate-humid climate with evenly-distributed annual precipitation without large spatial variations: annual precipitation is approximately 1, 200 mm; annual daily mean temperature is -4.8 °C in January and 21.9 °C in July (Kurczewski and Boyle, 2000). Additionally, there is no large spatial variation in topographical factors, such as elevation, slope and aspect within the study area (Fig. S3).

3. Methods

To measure forest recovery rate across a burn severity gradient, our workflow was composed of the following steps: data collections and preprocessing, WorldView-2 (WV-2)-based burn severity mapping, G-LiHT-based post-fire forest canopy species mapping, calculate post-fire

forest recovery rate, and quantify the relationship between post-fire forest recovery rate and burn severity (Fig. 3).

3.1. Data collections and preprocessing

NASA Goddard's LiDAR, Hyperspectral and Thermal (G-LiHT) data acquired on June 15, 2015, covering the partial burned areas (about 150 ha) at 1 m resolution (Fig. 2). G-LiHT uses a VQ-480 aerial laser scanning system (Reigl Laser Measurement Systems, Horn, Austria), and overlapping sampling swaths were used to obtain a mean pulse density of 15 to 20 laser pulses/m² (Cook et al., 2013), and the on-board IS sensor (Headwall Photonics, Fitchburg, MA, USA), ranging between the 407–1007 nm spectral region, provides 114 spectral bands at a 5 nm spectral resolution (full width half maximum) and a 12-bit radiometric resolution (Cook et al., 2013). In addition, G-LiHT has on-board profiling LiDAR, Global Positioning System and Inertial Navigation System (GPS-INS) and time server, data acquisition computer, and downwelling irradiance spectrometer, what enabling accurate multi-source data co-registration, radiometric normalization, and calculation of at-sensor reflectance product (Cook et al., 2013). At an altitude of about 200 m above ground with a 50° field of view, we conducted the 2015 G-LiHT-based aerial survey within 2-h window of local solar noon. The calibrated and georeferenced optical and LiDAR measurements at 1 m spatial resolution used in this study can be downloaded from the G-LiHT website (<http://gliht.gsfc.nasa.gov/>). To reduce the effects of variation in the illumination conditions during aerial data collections, we have performed cross-track illumination correction on the optical image in ENVI 5.3.

In addition to G-LiHT data in 2015, VHR WV-2 imagery acquired on July 17, 2011 and September 13, 2012 before and after fire was also available. Bi-temporal WV-2 imagery in 2011 and 2012 were first

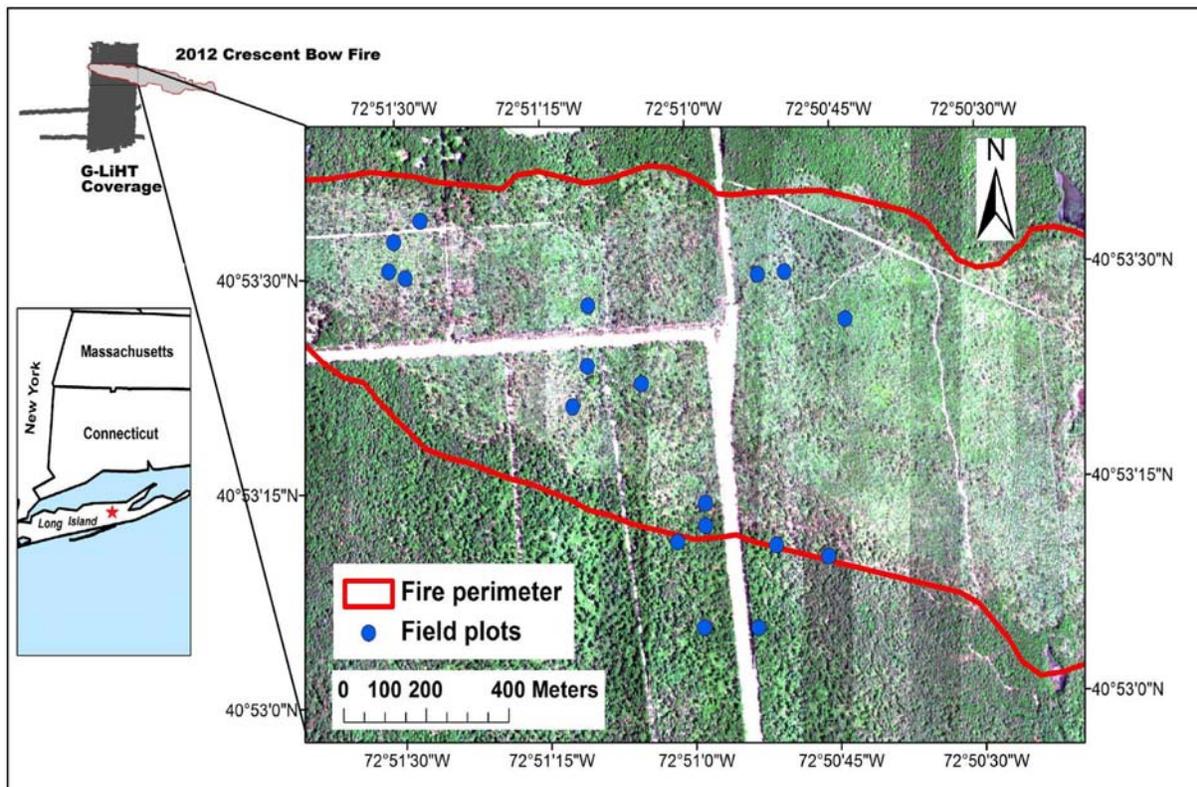


Fig. 2. The study area of a mixed pine-oak forest in Long Island, New York (the background imagery is the true color RGB composition (657 nm (red), 564 nm (green), and 484 nm (blue)) derived from NASA Goddard's LiDAR, Hyperspectral and Thermal (G-LiHT) measurements acquired on June 15, 2015). Insert graphs show the coverage of G-LiHT measurements and perimeter of Crescent Bow Fire occurred in April 2012, as well as the location of study site in Long Island. The center points of 18 15 m fixed-area plots including 212 crowns were also indicated on the map. (For interpretation of the references to color in this figure legend, the reader is referred to the web version of this article.)

ortho-rectified with a 10 m USGS digital elevation model (DEM), then co-registered and inter-calibrated to the G-LiHT at-sensor reflectance in 2015, as described in Meng et al. (2017). Then, using the Gram-Schmidt Spectral Sharpening (GSPS) method, we pan-sharpened the 2 m multi-spectral WV-2 images with the paired 0.5 m panchromatic WV-2 images to generate 1 m WV-2 images. In addition, centimeter-level ortho-rectified color aerial photos in May 2012 covering the burned areas were acquired from the New York Statewide Digital Ortho-imagery Program (<http://gis.ny.gov/>).

To map post-fire canopy species composition, during the spring of 2016, we collected forest inventory data from 18 15 m fixed-area plot at the crown level within the footprint of 2015 G-LiHT aerial measurement (Fig. 2). We measured individual tree crowns with > 2.5 cm diameter at breast height (DBH) of each fixed area plot, which resulted in 212 crown-level measurement including tree DBH, species, crown condition (vigor, defoliation, burned or dead), crown position (dominant, co-dominant, suppressed, or understory), canopy height, and crown base height (if applicable). Additionally, using a hand-held decimeter-level differential global positioning system (DGPS, Trimble Geo7x), we recorded the coordinates of fixed-area plot centers and all crowns with a horizontal accuracy of 0.3 m on average. For more details about field measurements, please refer to Section 2.3 in Meng et al. (2017).

To aid in the interpretation of potential problems of optical-only method (i.e., single spectral vegetation index) for post-fire recovery studies, we also convolved the G-LiHT reflectance imagery to simulate multi-spectral WV-2 imagery, according to the sensor response function in ENVI 5.3. Inter-calibrations were conducted between simulated WV-2 imagery in 2015 and bi-temporal WV-2 imagery in 2011 and 2012 to produce consistent temporal reflectance response, using Iteratively Reweighted Multivariate Alteration Detection (IR-MAD) method (Canty and Nielsen, 2008). Next, Modified Soil Adjusted Vegetation Index

(MSAVI, Table 1), having best performance in discriminating burned and unburned areas among eight different vegetation indices including NDVI at VHR (Table S1 & S2), was calculated for the WV-2 imagery in 2011 and 2012, as well as the simulated WV-2 imagery in 2015.

3.2. Map burn severity

We generated the burn severity map of Crescent Bow Fire, using the bi-temporal WV-2 imagery in 2011 and 2012. We first defined three levels of burn severity (i.e., low, moderate, and high; Fig. 4) according to the extent of tree canopy areas loss by fire via visual inspections on the post-fire 0.10 m aerial survey photos, which is consistent with traditional field interpretation of forest burn severity (Meng et al., 2017; Morgan et al., 2014). Although fire can cause multiple strata (e.g., soils, understory vegetation, and tree canopy) changes in forest (De Santis and Chuvieco, 2009), the extent of tree canopy area loss is a dominant factor in assessing burn severity in forests (Miller and Thode, 2007; Quintano et al., 2013; Veraverbeke et al., 2012). Then, using a multi-step classification method, we mapped the burn severity of Crescent Bow Fire at 1 m spatial resolution (Meng et al., 2017). Specifically, we first estimated the effectiveness of eight commonly used spectral indices to discriminate burned and unburned areas at VHR in our study area, and MSAVI shows the best performance (Tables S1 & S2; Meng et al., 2017). We thus used MSAVI to mask the unburned areas. Then, we implemented Multiple Endmember Spectral Mixture Analysis (MESMA; Roberts et al., 1998) on the post-fire WV-2 imagery in 2012 to derive fraction imagery including green vegetation (GV), non-photosynthetic vegetation or ash (NPV), and soil or other non-vegetation (NV). Finally, using MSAVI and MESMA-derived fraction imagery as predictors, we mapped three levels of burn severity with RandomForests (RF) method within the burned areas.

To quantify the relationship between burn severity and post-fire

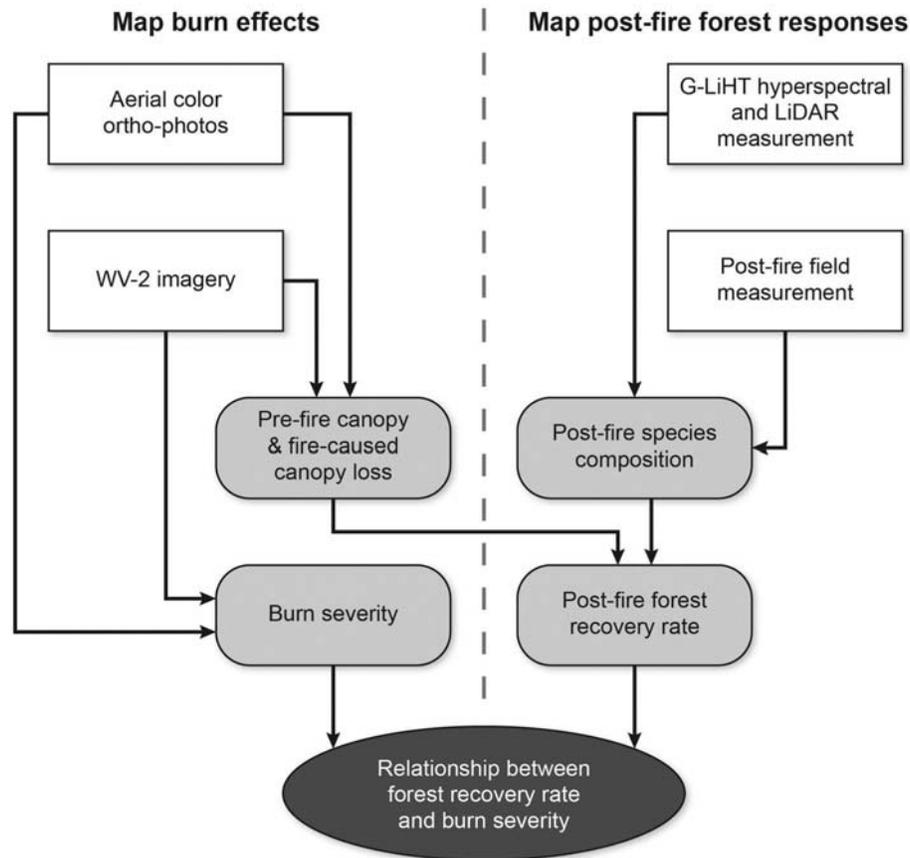


Fig. 3. Workflow in this study to quantify the relationship between burn severity and short-term forest recovery rate using multi-sensor remote sensing techniques.

Table 1
IS derived spectral indices used in this study.

Index	Equation (Red: R; Near-infrared: NIR)	Reference
Normalized difference vegetation index (NDVI)	$(R_{800} - R_{670}) / (R_{800} + R_{670})$	(Tucker, 1979)
Modified soil-adjusted vegetation index (MSAVI)	$\frac{2R_{NIR} + 1 - \sqrt{(2R_{NIR} + 1)^2 - 8(R_{NIR} - R_{RED})}}{2}$	(Qi et al., 1994)
Curvature index (CI)	$R_{685}^2 / (R_{675} \times R_{690})$	(Zarco-Tejada et al., 2001)
Vogelmann red edge index 1 (VREI1)	R_{740} / R_{720}	(Vogelmann et al., 1993)
Photochemical Reflectance Index (PRI)	$(R_{531} - R_{570}) / (R_{531} + R_{570})$	(Gamon et al., 1992)
Morres terrestrial chlorophyll index (MTCI)	$(R_{754} - R_{709}) / (R_{754} + R_{709})$	(Dash and Curran, 2007)
Carotenoid Reflectance Index (CRI)	$(1/R_{510}) - (1/R_{550})$	(Gitelson et al., 2002)
Renormalized Difference Vegetation Index (RDVI)	$(R_{800} - R_{670}) / (R_{800} + R_{670})^{0.5}$	(Roujean and Breon, 1995)
Red/Green Index (RGI)	R_{690} / R_{550}	(Zarco-Tejada et al., 2005)
Greenness index (GI)	R_{554} / R_{677}	(Zarco-Tejada et al., 2005)
Modified Chlorophyll Absorption Ratio Index (MCARI)	$[(R_{700} - R_{670}) - 0.2(R_{700} - R_{550})] / (R_{700} / R_{670})$	(Daughtry et al., 2000)

recovery rate (see Section 3.5), we further aggregated the fine-scale burn severity measurement in Meng et al. (2017) into a forest patch level. First, we created a 15 m grid in vector format with Qgis software covering the overlap areas of the G-LiHT footprint and fire perimeter, and this 15 m grid was used as a basis for the following analysis of this study. Then, based on zonal statistic method, we summarized the pixel number for each burn severity category and calculated the fraction of total 1 m high, medium, and low severity pixels in each 15 m grid cell (Fig. 4): forest burn severity measurement used in this study thus specially referred to the fraction of tree canopy loss by fire in fixed area grid of 15 × 15 m².

We chose a grid size of 15 m, because this represented the size of typical forest patches in our study area. By changing the grid size to 5 m, 10 m, 30 m, and 50 m, we conducted a sensitive analysis on the effect of varied grid size on the detected relationship between burn severity and post-fire forest recovery (Fig. S4, see Section 3.5).

3.3. Map post-fire forest canopy species composition

Non-vegetation areas (e.g., road, shadow, waterbody, and built areas) were first masked from the G-LiHT data in 2015 to retain well-lit vegetation pixels with an NDVI ≥ 0.70 and at-sensor NIR reflectance ≥ 10% for subsequent analysis (Marvin et al., 2016). Then, we conducted principle component analysis (PCA) on G-LiHT optical IS measurement and used the first three principle components (representing 99.9% of the variance in hyperspectral measurement) for post-fire forest canopy species (i.e., Standing dead, Pine, Oak, Canopy gap, Top-killed oak with resprout, and Non-vegetation) classification (Harsanyi and Chang, 1994). Additional, we calculated 11 spectral indices and extracted 37 structural metrics from G-LiHT data for classification (Tables 1 and 2).

PCA components and spectral indices were calculated in ENVI 5.3 software. Structural metrics were calculated using G-LiHT individual

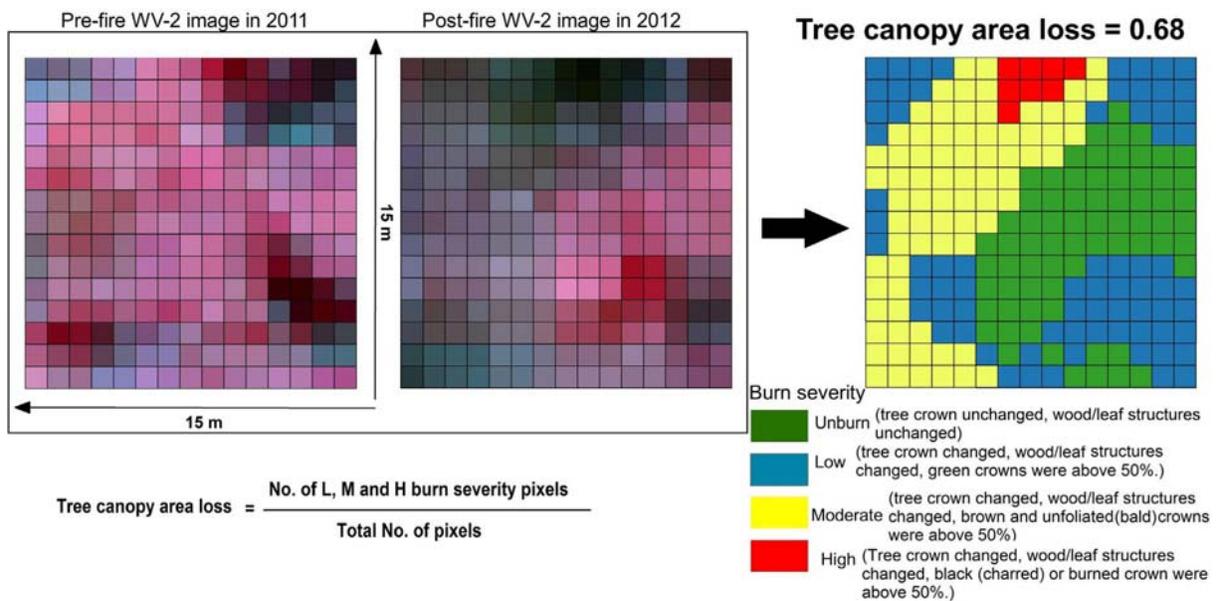


Fig. 4. Illustration of the procedure used to aggregate the fine-scale burn severity measurement (1 m ground-level resolution) by Meng et al. (2017) using bi-temporal WV-2 imagery (the background imagery is the false color RGB composition of WV-2 NIR-red-green band) to forest-patch level (i.e., tree canopy area loss measurement at 15 m ground-level resolution); following this procedure, we calculated the fraction of tree canopy area loss by fire in fixed area grid of $15 \times 15 \text{ m}^2$ and used it as a proxy of burn severity; the value range of burn severity here is 0 to 1. (For interpretation of the references to color in this figure legend, the reader is referred to the web version of this article.)

Table 2
LiDAR derived structural indices used in this study.

Index acronym	Description
CHM	Canopy height model, mean vegetation crown height
COV	Canopy cover, number of first returns above the cover cutoff (i.e., 5 m) divided by the number of all first returns and output as a percentage
DNS	Canopy density, number of all points above the cover cutoff (i.e., 5 m) divided by the number of all returns
QAV	Mean quadratic height, mean of the quadratic height ($\sum_{i=1}^n h_i^2/n$), h_i is the height of a return point and n is the number of all points
SKE	The skewness of all return points
KUR	The kurtosis of all return points
P10	10th percentile height value of return points between the ground and the maximum height
P20	20th percentile height value of return points between the ground and the maximum height
P30	30th percentile height value of return points between the ground and the maximum height
P40	40th percentile height value of return points between the ground and the maximum height
P50	50th percentile height value of return points between the ground and the maximum height
P60	60th percentile height value of return points between the ground and the maximum height
P70	70th percentile height value of return points between the ground and the maximum height
P80	80th percentile height value of return points between the ground and the maximum height
P90	90th percentile height value of return points between the ground and the maximum height
P99	99th percentile height value of return points between the ground and the maximum height
Int_min	Minimum intensities of return points
Int_max	Maximum intensities of return points
B10	Fraction of return points between the 10th percentile height and the maximum height (%)
B20	Fraction of return points between the 20th percentile height and the maximum height (%)
B30	Fraction of return points between the 30th percentile height and the maximum height (%)
B40	Fraction of return points between the 40th percentile height and the maximum height (%)
B50	Fraction of return points between the 50th percentile height and the maximum height (%)
B60	Fraction of return points between the 60th percentile height and the maximum height (%)
B70	Fraction of return points between the 70th percentile height and the maximum height (%)
B80	Fraction of return points between the 80th percentile height and the maximum height (%)
B90	Fraction of return points between the 90th percentile height and the maximum height (%)
0–1 m height class	The fractions of all points within the [0,1 m) height interval to the total number of points
1–2 m height class	The fractions of all points within the [1,2 m) height interval to the total number of return points
2–3 m height class	The fractions of all points within the [2,3 m) height interval to the total number of return points
3–6 m height class	The fractions of all points within the [3,6 m) height interval to the total number of return points
6–9 m height class	The fractions of all points within the [6,9 m) height interval to the total number of return points
9–12 m height class	The fractions of all points within the [9,12 m) height interval to the total number of return points
12–15 m height class	The fractions of all points within the [12,15 m) height interval to the total number of return points
15–20 m height class	The fractions of all points within the [15,20 m) height interval to the total number of return points
20–30 m height class	The fractions of all points within the [20,30 m) height interval to the total number of return points
30–40 m height class	The fractions of all points within the [30,40 m) height interval to the total number of return points

LiDAR return data (in the format of .las files) in Lastools software. Specifically, G-LiHT LiDAR point clouds were first binned into 1-m voxels, and then we calculated LiDAR structural indices and converted them into individual raster. According to the structural characteristics of our study area, a 5 m canopy height threshold, which is 35% of the average canopy height of the unburned area, was applied to calculate canopy related LiDAR metrics. These spectral indices and LiDAR structural metrics, as well as PCA components, have been used extensively for remote sensing of vegetation health and species in previous studies (e.g., Fassnacht et al., 2016; Shendryk et al., 2016). Details about spectral indices and structural metrics used in this study can be found in Tables 1 and 2, respectively.

We first overlaid the geo-referenced points of individual trees, derived from field inventory data, directly on the RGB composition of G-LiHT optical and LiDAR Canopy Height Model (CHM) imagery. Then, with the help of historical (2010–2016) VHR imagery in Google Earth Pro (<http://www.google.com/earth>) and our knowledge about the study areas, we manually extracted training samples, avoiding shade and edge areas, for mapping post-fire canopy species composition, directly on the G-LiHT imagery, as these forest canopy species demonstrate contrasting color, texture, structure, and cluster patterns. In total, this yielded 383 usable samples for training (60%) and validation (40%) of the post-fire canopy species classification in 2015. RF decision tree nonparametric classifications were used in this study, because RF classifications make no assumption on the underlying data distribution and are widely used for remote sensing studies (e.g., Breiman, 2001; Meng et al., 2012; Meng and Dennison, 2015; Pal, 2005; Yu et al., 2011). RF classifications were performed with “RandomForests” package and important predictor variable selection with “varSelRF” package in R environment.

Based on training samples, a backward method was performed to select most important predictor variables for the post-fire canopy species classification in 2015, according to RF variable importance estimation for 500 random models. Specifically, using RF Out Of Bag (OOB) error as a criterion, backward method starts all available optical or LiDAR predictors for RF modeling (Tables 1 & 2), and then removes the predictor with the least contribution to improve classification (i.e., no or slight increase in accuracy) until all left predictors contribute significantly to the RF model. Provided by RF model, OOB error is an internal unbiased estimate of the training error (Breiman, 2001). By dropping unnecessary variables, variable selection can increase the classification accuracy and reduce the computation time and the chance of over-fitting (Fassnacht et al., 2016; Meng and Dennison, 2015). To explore the added value of combined use of optical and LiDAR data in classification, we repeated the process of important predictor variables selection for optical, LiDAR, and optical + LiDAR variables, separately. Then, we compared the training accuracies of the three trained RF models.

The trained RF model with the selected most important optical and LiDAR predictor variables (showing best performance during RF training process, see Section 4.1) was applied to classify six post-fire canopy species in 2015 across the study area. A 3 by 3 majority filter was applied to remove outliers or impulse-like noises on the RF classification map in ENVI 5.3, what is a common post-classification procedure for accuracy improvement (Quintano et al., 2013). Based on the validation samples, the classification accuracies were finally assessed, and the Overall Accuracy (OA), Producer's Accuracy (PA or omission error) and User's Accuracy (UA or commission error) for each class (excluding non-vegetation class) were also calculated with a confusion matrix.

3.4. Calculate post-fire forest recovery rate

Following the burn severity and post-fire forest canopy species mapping, post-fire forest recovery rates at community and species level were calculated according to the Eq. (1) and Eq. (2), respectively.

$$\text{Community level recovery rate} = \frac{\sum_{i=1}^n \Delta A_i}{Y_n \times \sum_{i=1}^n A_{i,2011}} \quad (1)$$

$$\text{Species level recovery rate} = \frac{\Delta A_i}{Y_n \times A_{i,2011}} \quad (2)$$

where ΔA_i is the change in canopy area (%) for species i , Y_n is the number of years after the fire in certain size grid (i.e., 15 m), n is the number of tree species (i.e., pine and oak here), and $A_{i,2011}$ is the fraction of pre-fire canopy area for species i in the same size grid. Post-fire forest recovery rate calculated here thus referred to the percentage of increase in tree canopy area per year in fixed area grid of $15 \times 15 \text{ m}^2$.

Here we assumed that the post-fire forest recovery occurred within the areas of forest canopy loss caused by fire, thus change in canopy area (ΔA_i) within these areas during the post-fire period can be used for calculating post-fire forest recovery rate. To estimate change in canopy area (ΔA_i) after the fire, a map of forest canopy loss caused by fire was first generated, based on the 2012 WV-2 MESMA results and the burned area map (See Section 3.4 in Meng et al., 2017), to mask forest canopy areas in 2012 after the fire. We didn't directly use the burned area map generated in Meng et al. (2017) for estimating change in canopy area (ΔA_i), because the detected burned area might still include tree canopy areas. Based on the MESMA results in Meng et al. (2017), we defined the 2012 WV-2 imagery pixels within burned area map as forest canopy loss caused by fire that met either of two conditions: 1) pixels were successfully unmixed by pure green vegetation and non-photosynthetic vegetation, ash, and char endmembers excluding oak or pine; 2) the unmixed contributions of oak or pine endmember were < 50% during the MESMA (Meng et al., 2017). The accuracy of the map of forest canopy loss caused by fire was assessed by visual inspections of 0.10 m color aerial ortho-photos in 2012 and the historical (2010–2016) VHR imagery in Google Earth Pro. To control for observation bias, the visual inspections for validation were conducted by an independent observer. Fifty validation points per class (i.e., forest canopy vs. non-forest canopy) were randomly generated through stratified sampling within the overlap area of fire perimeter and G-LiHT coverage. An overall accuracy of 90% was estimated by a confusion matrix, and User and Producer's Accuracy (UA and PA) were relatively high (> 80%) for both canopy and non-canopy classes (Table S3).

Then, after applying the map of forest canopy loss caused by fire to the 2015 post-fire canopy species composition map, change in canopy area (ΔA_i) at both community level and species level were calculated separately by counting forest canopy pixels within each cell in 15 m grid, and corresponding recovery rates for the study post-fire period (i.e., 2.75 years, September 2012 to June 2015) were finally calculated according to Eq. (1) and (2). Additionally, we calculated the resprout rate of top-killed oak with resprout according to Eq. (2), but considered it as understory recovery in this study, because it represents a different succession state, compared to survived tree canopies (Reich et al., 1990).

The fraction of pre-fire species-specific canopy area ($A_{i,2011}$) was incorporated in Eqs. (1) and (2) to avoid the effects of different pre-fire canopy areas on quantifications of relationships between post-fire forest recovery rate and burn severity. Similarly, the fraction of pre-fire canopy area was calculated by counting species-specific canopy pixels within each cell in 15 m grid (total 125 pixels). The pre-fire canopy species composition (i.e., pine and oak) were classified, based on the 2011 WV-2 imagery using a RF approach (Liaw and Wiener, 2002). According to the confusion matrix-based validation, the pre-fire canopy species classification had an overall accuracy of 73% (Table S4). For details about the pre-fire forest species classification and validation procedure, please refer to Section 1 in Supporting Information.

To study the added value of combining optical and LiDAR measurements for estimating post-fire forest recovery rate, we also calculated post-fire forest recovery rate by optical-only method at the canopy

community level. Specifically, the optical-only post-fire recovery rate (i.e., change in MSAVI per year) was estimated by averaging changing MSAVI values of change in canopy area (ΔA_i) within each cell in 15 m grid from 2012 to 2015.

Because the fraction of pre-fire canopy area ($A_{i,2011}$ in Eq. (1)) can be lower to zero, infinite values were possible during the calculation of post-fire recovery rate. Thus, to remove the effects of infinite values, we assigned a threshold of 0.2 to $A_{i,2011}$ for further data analysis. This threshold was determined by a sensitivity analysis on the effects of $A_{i,2011}$ on the detected burn severity-post-fire forest recovery rate relationship. Specifically, we repeatedly changed the value $A_{i,2011}$ in Eq. (1) from 0.1 to 0.4 with an equal interval of 0.1 for quantifying relationships between forest recovery rate and burn severity. Then, we found the relationships became consistent in terms of shape and magnitude, when $A_{i,2011}$ larger than 0.2 in 15 m grid (Figs. S5, S6, and S7). As a result, post-fire recovery rates at both canopy community and species level in this study were finally calculated with $A_{i,2011}$ of ≥ 0.2 in 15 m grid.

3.5. Quantify the relationship between burn severity and post-fire forest recovery rate

Using burn severity as a single predictor variable, we built separate Ordinary Least Square (OLS) models to predict post-fire forest recovery rates, as well as oak resprout rate, at both community and species level. Specifically, to reduce noise, we first considered each 15-m grid cell as a single data point and binned all of 15-m grid cells into different bands (i.e., twenty bands in total, such as 0–0.05, 0.10–0.15, ... 0.95–1.00) with an equal interval of 0.05, according to their associated burn severity measurement (i.e., fraction of canopy loss by fire from 0 to 1). Then, we calculated the mean and standard error of post-fire forest recovery rate of each binned band. Finally, we build OLS models to predict the mean values of recovery rate of each binned band, as a function of mean value of burn severity of each binned band. To compare performances of combined use of optical and LiDAR measurement with that of optical-only one, we further applied the same OLS modeling process to predict post-fire recovery rates measured by optical-only variable (i.e., MSAVI) from 2012 to 2015 at the canopy community level. We performed all statistical analyses in R environment.

To explore the uncertainty caused by grid size for data analysis, we conducted a sensitivity analysis on the effects of grid size on quantifications of relationships between post-fire recovery rate and burn severity. Specifically, we generated multiple grids with varying size of 5 m, 10 m, 30 m, and 50 m covering the same area as 15 m grid, and then re-calculated the relationship between burn severity and post-fire recovery rate with different grid size using the same methodology presented here. We found out that the variation in grid size didn't change the general pattern of the detected burn severity-post-fire recovery rate relationship (Fig. S4).

4. Results

4.1. Post-fire forest species classification in 2015

The in situ photographs taken in June 2015 show several post-fire forest canopy species we mapped in this study (Fig. 5, the live oak canopy and non-vegetation class not included, see Fig. S8 for oak spectral and structural properties). About three years following the fire, forest canopies were still open because of high burn severity. Trees killed immediately by burn (charred) or delayed mortality (remained bald crowns) during the post-fire period were both common; live trees already started to foliate new leaves; pitch pine seedlings were very rare within our field plots (i.e., $< 0.1\%$); top-killed oak had dense resprout from root crowns; live oak canopies were rare at moderate-high severity areas (See Section 4.2 below).

We found that G-LiHT measurements were able to capture the spectral and structural properties of these post-fire canopies (Fig. 5b). In the red-edge to NIR wavelengths, live oak canopies displayed the highest reflectance values (NIR mean of 0.27 ± 0.015), followed by the top-killed oak with resprout (NIR mean of 0.24 ± 0.011); in contrast, pine canopies had the lowest overall reflectance values (NIR mean of 0.19 ± 0.011), including when compared with canopy gap areas likely due to the dominance of herbaceous and broadleaf shrub vegetation in the canopy gaps, with higher NIR reflectance values (NIR mean of 0.21 ± 0.006). Standing dead canopies demonstrated much higher reflectance in the visible wavelengths (VIS mean of 0.04 ± 0.002), because of non-photosynthetic materials, but still showed relatively high reflectance values in the NIR wavelengths (NIR mean of 0.18 ± 0.009), due to the exposed understory beneath the dead canopies. In terms of vertical structure, pine canopies demonstrated large differences in vertical distributions of return laser points, compared with the standing dead trees and canopy gap (Fig. 5c). In addition, unique structural characteristics of top-killed oak with resprout were captured by the G-LiHT LiDAR measurements. Most of the vertical distributions of return laser points for canopy gap were below 1 m height, significantly different from other classes.

According to the result of importance variable selections, 5 of 37 LiDAR-derived predictor variables and 5 of 12 IS-derived predictor variables were used for the final post-fire canopy species classification (See Section 4.2) for the 2015 imagery (Fig. S9). With our LiDAR-derived predictor variables, the most important variables for mapping post-fire canopy species included CHM, B70, 0–1 m height class, B10, QAV, and B60; as to IS-derived predictor variables, PRI, PCA2, VREI1, CI, and CRI were selected.

The RF training results show that the combined use of optical and LiDAR measurements tend to have better overall performances in canopy species classification than using either of them alone (Fig. S10, increase to 80% from 70% or 73%). In general, optical predictor variables have higher training accuracy than LiDAR predictor variables, but have lower accuracy in discriminating the canopy gap and standing dead classes. Specifically, pine has the largest increase in training accuracy (57% to 78%), when using combined optical and LiDAR predictor variables; the training accuracy of standing dead is still relatively low, even when leveraging the two data streams together (63%).

We used validation samples to calculate OA, PA, and UA of the post-fire canopy species map (See Section 4.2) by the combined use of optical and LiDAR measurement (Table 3). The OA of the post-fire canopy species map were 88%. Oak, pine, and canopy gap had relatively high values in UA ($> 80\%$) and PA ($> 80\%$), because of their apparent spectral and structural characteristics (Fig. 5). Standing dead class had overall lowest values in UA (62%) and PA (67%), caused mainly by the confusion with top-killed oak with resprout; top-killed oak with resprout had acceptable accuracy in UA (72%) and PA (70%). In summary, the improved accuracy for species differentiation by the combined use of optical and LiDAR measurement (Fig. S10) was consistent with recent studies (Alonzo et al., 2014; García et al., 2011; Martin-Alcon et al., 2015; Naidoo et al., 2012).

4.2. Spatial patterns of post-fire forest canopy species and community-level recovery rate in 2015

About three years after the fire, the post-fire forest canopy species map in 2015 as well as community-level recovery rate map still demonstrates strong spatial covariations with the burn severity map in 2012 (Fig. 6). For example, at high burn severity areas (e.g., R2-C3, R3-C5; Fig. 6a), canopies were dominated by canopy gap, standing dead trees, and top-killed oak with resprout (Fig. 6b), thus corresponding recovery rates were low (Fig. 6c); at moderate burn severity areas (e.g., R2-C2, R3-C4; Fig. 6a), the distributions of oak and pine canopies became more frequent (Fig. 6b) and recovery rates were also higher (Fig. 6c); although unburned-lower burn severity areas (e.g., R1-C5,

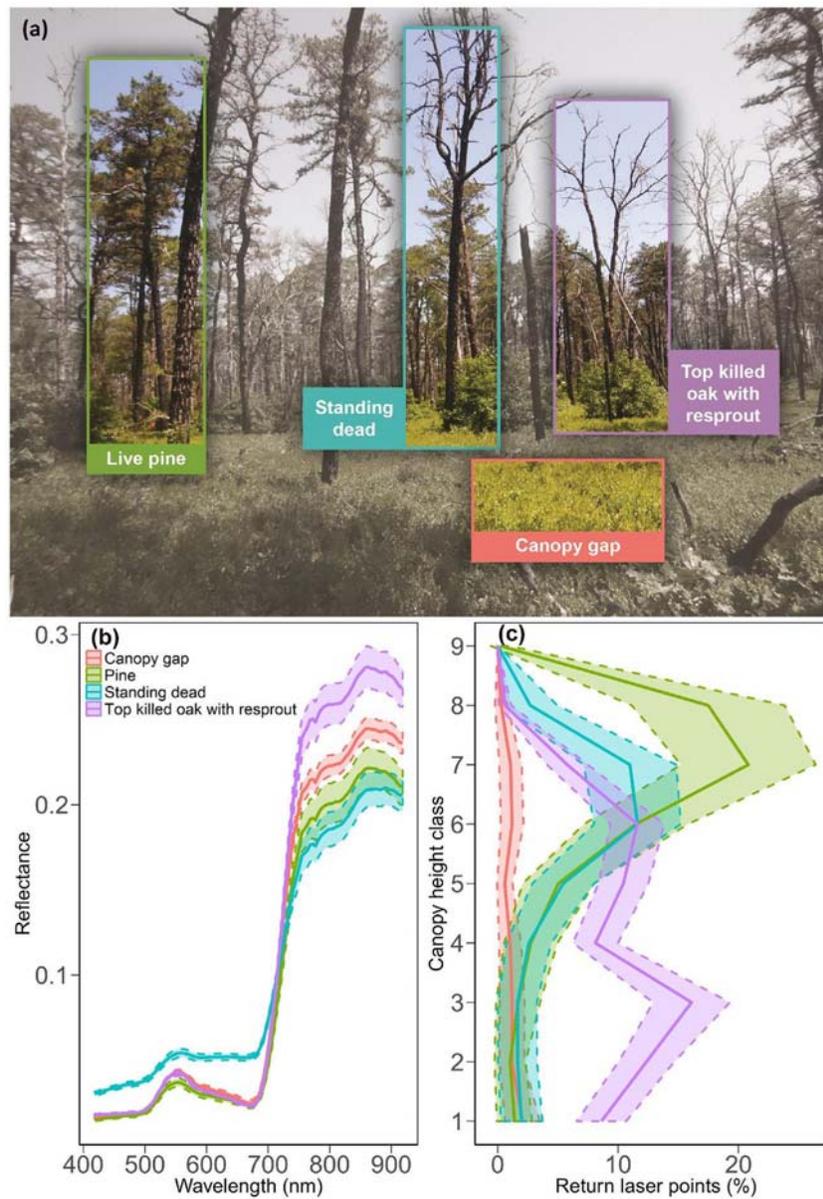


Fig. 5. Post-fire forest canopy characteristic across a burn severity gradient: (a) An in situ photography taken in June 2015; (b) Spectra derived from NASA Goddard's LiDAR, Hyperspectral and Thermal (G-LiHT) measurements acquired on June 15, 2015; (c) Vertical structures derived from G-LiHT LiDAR measurements (canopy height class: 1: [1-2 m); 2: [2-3 m); 3: [3-6 m); 4: [6-9 m); 5: [9-12 m); 6: [12-15 m); 7: [15-20 m); 8: [20-30 m); 9: [30-40 m)]. Shade areas shows 95% confidence interval (See Fig. S8 for spectra and structural properties of oak canopies). (For interpretation of the references to color in this figure legend, the reader is referred to the web version of this article.)

R3-C1; Fig. 6a) were covered by dense oak and pine canopies, forest recovery rates were still low, because of little canopy loss by fire. Moreover, compared with oak canopies, the distribution of pine

canopies was much more frequent across the high-moderate severity areas, indicating the varied post-fire tree responses with different fire adaptive strategies (see Section 4.4).

Table 3
Confusion matrix of postfire canopy classification.

		Reference data					User's accuracy (%)
		Canopy gap	Oak	Pine	Top-killed oak with resprout	Standing dead	
Classification result	Canopy gap	24	0	0	0	0	100
	Oak	0	49	0	1	0	98
	Pine	0	3	47	3	1	87
	Top-killed oak with resprout	0	2	3	21	3	72
	Standing dead	0	0	0	5	8	62
Producer's accuracy (%)		100	91	94	70	67	
Overall accuracy (%)		88					

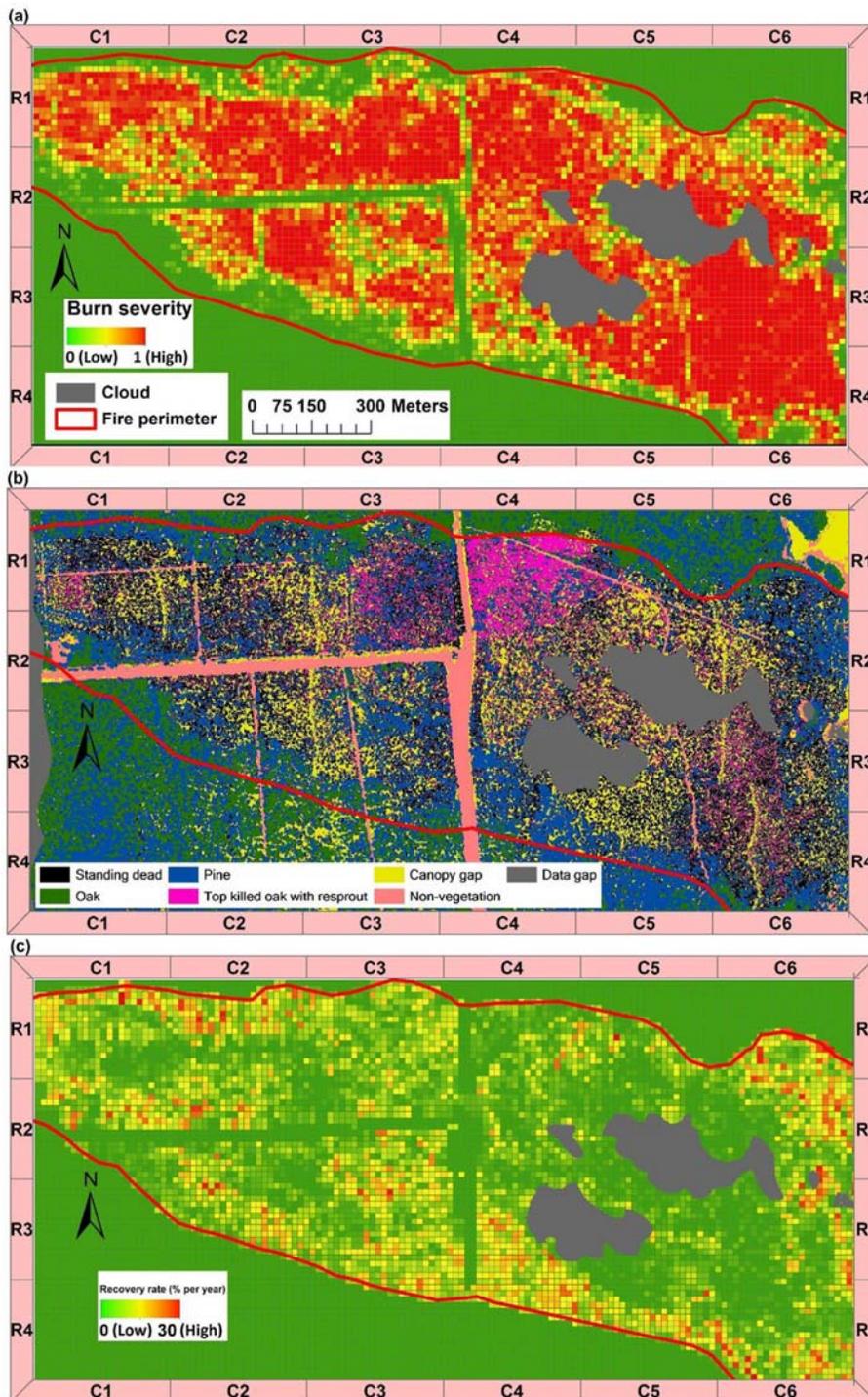


Fig. 6. Assessing forest recovery rate-burn severity relationships in a mixed pine-oak forest: (a) Burn severity measurement at 15 m resolution using bi-temporal WorldView-2 (WV-2) imagery, acquired on July 17, 2011 and September 13, 2012; The value range of burn severity here is 0 to 1, referring to the fraction of tree canopy area loss caused by fire in each 15 m grid cell; (b) Post-fire forest canopy species map in 2015 at 1 m resolution by NASA Goddard's LiDAR, Hyperspectral and Thermal (G-LiHT) measurement, acquired on June 15, 2015; (c) Community level forest recovery rate (i.e., canopy area-based percent increase per year, see Section 3.4 for details) map at 15 m resolution from September 13, 2012 to June 15, 2015. (For interpretation of the references to color in this figure legend, the reader is referred to the web version of this article.)

4.3. Community-level post-fire forest recovery as a function of burn severity

Through the combination of G-LiHT optical and LiDAR measurement with WV-2 imagery, we detected a convex relationship between post-fire forest recovery rate and burn severity, with a maximum recovery rate of 10% per year, indicating the existence of a threshold in forest response to fire (adjusted $R^2 = 0.96$, p -value < 0.001, Table S5; Fig. 7a). The forest recovery rate first shows an increase with burn severity, followed by a decline after a peak burn severity (0.575 in this study, Fig. 7a), likely due to increased fire-induced tree mortality. As with previous traditional remote sensing approaches (Fig. 1b and Fig. S2), the post-fire MSAVI recovery rate demonstrated a steadily

increasing trend with burn severity (adjusted $R^2 = 0.67$, p -value < 0.001, Table S5; Fig. 7b), signifying a trend of post-fire apparent recovery across a burn severity gradient. This is because the differences between post-fire forest and understory recovery can be hardly distinguished by single spectral vegetation index, like MSAVI.

4.4. Species-specific post-fire forest recovery as a function of burn severity

The convex relationship between post-fire forest recovery rate and burn severity also held at the species level (Fig. 8a & b). However, we also observed important differences in the maximum recovery rate with corresponding burn severity between the oak and pine canopies.

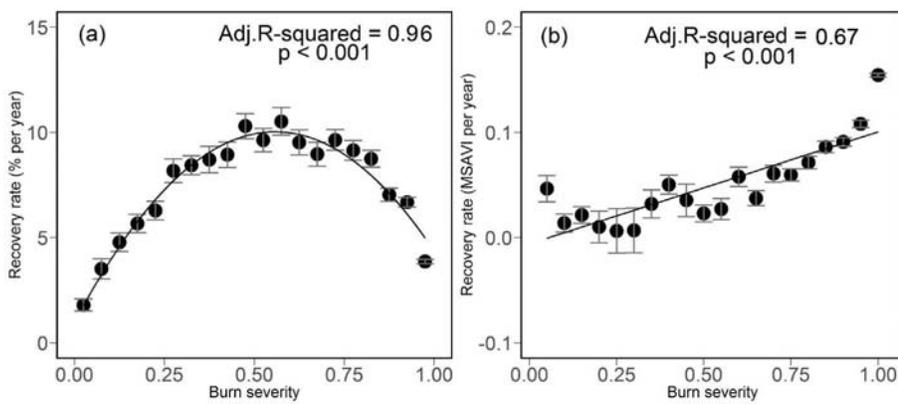


Fig. 7. The canopy community level forest recovery rate-burn severity relationships (see Section 3 for calculation method): (a) Combined use of optical and LiDAR; (b) Optical-only (i.e., MSAVI; see Table 1 for details). Dot points are the mean, vertical bars are standard error, black lines are the binomial (linear) fitting curves based on mean values of each burn severity band used for result compilation, adjusted R-squared values are also shown here (see Table S5 for detailed modeling results).

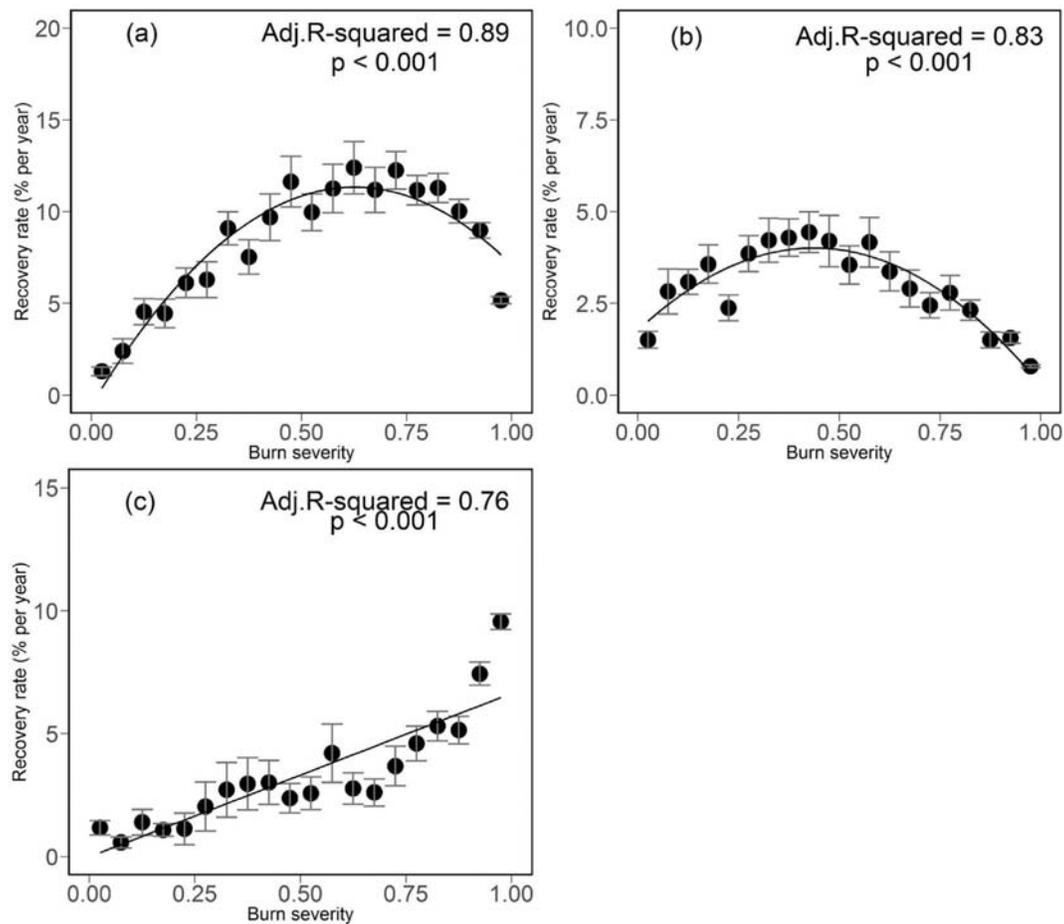


Fig. 8. The species-specific forest recovery rate-burn severity relationships by the combined use of optical and LiDAR measurement (see Section 3 for calculation method): (a) Pine; (b) Oak; (c) Oak resprout after top killed (i.e., oak understory recovery). Dot points are the mean, vertical bars are standard error, black lines are the binomial (linear) fitting curves based on mean values of each burn severity band used for result compilation, adjusted R-squared values are also shown here (see Table S5 for modeling results).

Specifically, we found a maximum recovery rate for pine canopies of about 12% per year, which was nearly three times larger than that of oak canopies at about 4% per year. In addition, the burn severity of trend changing for pine is 0.625, which is much larger than oak (i.e. 0.425), indicating stronger fire resistance of pine stands. We also detected a positive linear relationship between the post-fire oak resprout rate and burn severity, with a maximum resprout rate of nearly 10% per year (Fig. 8c), suggesting the unique fire adaptive strategy of oak trees.

5. Discussion

Understanding the quantitative relationship between post-fire forest

recovery and burn severity over broad spatial scales is an essential first step for the accurate model representation of fire effects on forest dynamics and global carbon cycling under a changing climate (Fisher et al., 2015; Gu et al., 2016; Hantson et al., 2016; Huang et al., 2013; Turner, 2010; Yang et al., 2017). In this study we leveraged multi-scale and multi-sensor remote sensing observations and techniques (e.g., co-aligned airborne IS and LiDAR measurements, VHR satellite multi-spectral imagery) to explore post-fire forest recovery rate in a spatially explicit manner spanning a large gradient in burn severity about three years after a fire. Through our work we observed a comparable convex relationship between forest recovery rate and burn severity across our study area (Fig. 7a), which is consistent with field scale research (e.g.,

Balch et al., 2011; Smith et al., 2016), as well as post-fire forest recovery studies across larger spatial-temporal scales (Zhao et al., 2016). Additionally, our work highlighted that the detected patterns also held at the species level, but their shapes (including maximum recovery rate and corresponding burn severity) varied across species (Fig. 8). These detected patterns suggest the species-specific fire adaptive strategies, as well as burn severity, can affect post-fire forest recovery process and should be incorporated into fire effect schemes in ecological process models (Fisher et al., 2015; Hantson et al., 2016). Moreover, the novel methodology presented here could provide valuable input and benchmark datasets for informing and evaluating process models across space and time.

The detected convex relationship is consistent with previous field-based expectations, but does not agree with our analysis leveraging optical-only single spectral vegetation index (i.e., MSAVI, Fig. 7). Fig. 7b shows that our optical-only analysis leads to a linear, positive relationship between forest recovery rate and burn severity. We note it is important to differentiate here between an evaluation based on time-since-fire and burn severity, where the later shows the impact of burn severity on short-term recovery (Figs. 1, 7, and 8), while time-since-fire would show a different pattern more related to overall canopy greenness (Bastos et al., 2011; Chen et al., 2011; Fernandez-Manso et al., 2016; Meng et al., 2015). This is driven by the fact that single spectral vegetation index cannot separate vegetation recovery of upper strata from that of lower strata, which often results in an unrealistic rapid forest recovery under high burn severity (Fig. 1a, Fig. S2; e.g., Balch et al., 2011; Brando et al., 2012; Meng et al., 2015; Serbin et al., 2013; Smith et al., 2016). However, the combined use of optical and LiDAR measurement for quantifying post-fire forest recovery rate can overcome this limitation (Figs. 7a and 8). Specifically, IS in this study can record variations in canopy spectral signatures with high spatial and spectral resolution (Cook et al., 2013), enabling canopy species identification at VHR (e.g., Clark et al., 2005); on the other hand, LiDAR remote sensing provides precise measurements of the vertical canopy structure and is capable of differentiating upper from lower canopy strata (e.g., Tang and Dubayah, 2017; Fig. 5). The additional structural characteristics of post-fire canopies from LiDAR measurements can also enable more accurate species identification (Fig. S10; Fassnacht et al., 2016), and thus improve the characterization of species-level post-fire response (e.g., top-killed oak with resprout), at least in our relatively simple ecological system, but would also likely translate to other similar systems such as fire-prone boreal forests. Similar to the optical-only method (Fig. 7b), our additional analysis also indicated the limitations of a LiDAR-only method to quantify the relationship between post-fire forest recovery and burn severity (Fig. S11), likely because the LiDAR-only measurements cannot efficiently differentiate healthy, green canopies from oak resprouting or snags. However, further studies with multi-temporal consistent LiDAR measurements are still needed to draw a decisive conclusion here.

Our remotely sensed characterization of the species-specific post-fire responses to variation in the degree of burn severity indicated that pine stands in our system tended to have higher post-fire forest recovery rates than the oaks, while oak stands tended to have much faster understory recovery, owing to the ecological adaptation to re-sprout from the root collar, after a top-killing fire during the short-term post-fire period (Fig. 8). This finding quantitatively supports previous field-based studies in similar mixed pine-oak ecosystems indicating that both oak and pine are fire-adapted but with differential fire adaptive strategies, including vigorous resprout from the root collar vs. thick fire-resilient bark with pine trees (e.g., Little, 1998; Whittaker and Woodwell, 1969). The epicormic branching of dominant pitch pine makes fast forest canopy recovery during the short-term period possible, which might not be visible for decades in other pine dominated fire-prone ecosystems relying regeneration from seedbanks (e.g., Lodgepole Pine or Jack Pine) (Bolton et al., 2015; Nelson et al., 2016; Sharpe et al., 2017; Zhao et al., 2016). Also likely because dense and

fast shrub recovery inhibited the shade-intolerant seedlings or our short-term post-fire study period (Motzkin et al., 1999), seedling recovery was rare in our study area and we thus haven't fully separated understory shrub or non-woody recovery from understory seedling recovery. However, given the underlying relationship between forest status and spectral and structural properties (Caughlin et al., 2016; Sparks et al., 2016), and the growing evidence that canopy-level spectral and structural properties can be quantified from VHR IS and LiDAR data (Caughlin et al., 2016; García et al., 2011; Torabzadeh et al., 2014) (Fig. 5, including this study), we believe our proposed methods have strong potential to accurately quantify forest recovery rate or understory seedling recovery rate, across a burn severity gradient in other ecosystems not just during the short-term post-fire period. Thus, our study demonstrates that the value of leveraging multi-sensor remote sensing techniques to quantify species-specific post-fire responses over large spatial-temporal scales (Fig. 1c), which is tightly connected with the underlying fire adaptive strategies (Keeley et al., 2011; Pausas and Keeley, 2014; Pausas et al., 2016). However, we also note that in addition to species and burn severity factors under study, some other factors, such as soil, topography, and post-fire climate, can also affect post-fire forest recovery rate (e.g., Meng et al., 2015; Zhao et al., 2016), which can likely result in varying long-term (≥ 5 years) recovery rates between seedling and resprouting species at areas with large variations in soil, topography and post-fire climate.

We also acknowledge the uncertainties that remain in this study. First, due to data availability we quantified the post-fire forest recovery rate by integrating the pre and post-fire WV-2 imagery with our additional post-fire G-LiHT measurement in 2015 (Fig. 3). This could introduce errors due to inconsistency in remote sensing spectral bands or accuracies of derived remote sensing products (Table 3, Table S3, and Table S4), which could increase the uncertainty of our detected post-fire forest recovery pattern. However, this limitation is also a strength of our approach showing that despite the differences in sensors, we were able to leverage our novel method to build a strong model of forest recovery, consistent with field expectations. Our analysis showed that WV-2 bands and G-LiHT IS have almost identical performances for measuring post-fire forest recovery across a burn severity gradient (Fig. S12), suggesting that G-LiHT IS data in 2015 can achieve comparable results as if that of WV-2 used in 2015. Additionally, G-LiHT data in 2015 also includes LiDAR observations that allow us to characterize forest structure, which we didn't expect to change significantly about three years after the fire, particularly in terms of differentiating tree canopies from understory vegetation. Second, we acknowledge that some uncertainties may also have arisen when simulating WV-2 imagery from the G-LiHT IS in 2015 (Section 3.1). However, simulating coarser spectral resolution spectra from finer spectral resolution sensor have been widely applied and successfully used for remote sensing studies (Hochberg and Atkinson, 2003; Liu et al., 2017). Therefore, our detected post-fire forest recovery pattern across a burn severity gradient using multi-sensor remote sensing measurements should be reliable.

On the other hand, leveraging multi-sensor remote sensing measurements for environmental studies will become more and more important, as the fast development and increasing availability of multi-sensor remote sensing measurements (Stavros et al., 2016; Torresan et al., 2017). As a result, despite the potential for additional uncertainty it is also important to utilize all available data to inform our understanding of ecological patterns and we have shown here how a multi-platform, multi-sensor approach can be used to study post-fire recovery. Thus, we recommend further study on the use of multiple sources of information to explore fire effects on vegetation canopies in similar and other ecosystems (e.g., chaparral, grassland, and other forests).

Our study also has three important implications. First, our finding of forest recovery rate as a function of burn severity would help to parameterize and validate the fire effect schemes in ecological process models, where it would enable improved representation and projection of fire-vegetation interactions to global change (Hantson et al., 2016;

Lasslop et al., 2014; Seidl et al., 2011; Turner, 2010; Yang et al., 2017). For example, ecological process models with gap-based vegetation-fire scheme, including species-specific recovery trait parameter, have been proposed to simulate post-fire forest recovery (Fisher et al., 2015; Yang et al., 2017). However, large-scale benchmark datasets to parameterize and validate the models of this kind are largely lacking. The success to link remote sensing techniques to quantify species-specific post-fire forest recovery as shown in our study provides a very promising avenue to constrain and benchmark the ecological models of this kind.

Second, our study highlights a promising new avenue for forest management by providing a quantitative description of forest recovery rate in a spatially explicit manner. As with other previous studies of fire-induced forest changes using repeat airborne LiDAR measurement from LiDAR (Alonzo et al., 2017; McCarley et al., 2017; Zhao et al., 2018), our work provides new insights regarding the fate of disturbed trees during the post-fire recovery period. For example, we were able to quantify the understory recovery of oak trees (oak resprout; Figs. 5 and 8c), which can exert large impacts in shaping forest structure and function dynamics during post-fire succession (Jordan et al., 2003; Kurczewski and Boyle, 2000). As a result, monitoring large-scale forest dynamics in a spatially explicit manner could provide critical information to aid in the management of forests in a timely and precise manner (e.g., prescribed burning, post-fire rehabilitation) for multiple uses (e.g., preserve and restore the endangered fire-dependent ecosystems, timber harvest, and recreation; Jordan et al., 2003).

Third, our novel approach to examining post-fire recovery in a spatially explicit manner may also enable the remote detection of other disturbance-induced forest dynamics (e.g., drought, windstorm, and insect herbivory), which are also important given increasing frequencies and intensities of various other forest disturbance activities with continued global change (Barbero et al., 2015; Schwalm et al., 2017; Westerling et al., 2006). This is primarily because that the similar convex forest recovery response also exists in various other disturbance events, such as drought (Levesque et al., 2013; Schwalm et al., 2017; Zweifel et al., 2009) and windstorm disturbance (Papaik and Canham, 2006; Rich et al., 2007). Differentiating forest canopy recovery from understory recovery is equally important in these post-disturbance studies, and different species also would exert differential convex responses. The improved representation of forest recovery–disturbance extent relationship in ecological process models can largely reduce uncertainties in simulating disturbance effects on global carbon cycle and their feedbacks to the climate system (Kurz et al., 2008; Rogers et al., 2015; Turner, 2010). Therefore, we expect that our proposed method can also be extended to other disturbance events.

6. Conclusion

In our study we successfully mapped the spatial pattern of short-term post-fire forest recovery rate and quantified its relationship with burn severity in a mixed pine-oak forest over large-scales, by leveraging multi-sensor remote sensing techniques (e.g., 1 m simultaneous airborne IS and LiDAR and 2 m satellite multi-spectral imagery). Additionally, we presented a new method for quantifying species-specific post-fire forest recovery rate (oak vs. pine) to different levels of burn severity with remote sensing techniques, as one of the first quantitative evidences showing the effects of fire adaptive strategies on post-fire forest recovery, derived from large spatial-temporal scales. Such monitoring of forest recovery over large-scales in a spatially explicit manner not only can provide novel insights about fire effects on forests (Alonzo et al., 2017; McCarley et al., 2017), but also unique opportunities for further study of forest ecological, structural, and functional responses to fire (e.g., specific leaf or stem traits that relate to plant resistance to and recovery capacity from fire), which are of high interest in the carbon and water cycle and forest management communities (Bolton et al., 2017; Johnstone et al., 2011; Lewis et al., 2006; Mayor et al., 2007; Turner et al., 1998; Turner et al., 1997;

Turner et al., 2016). Our novel method could also be extended to quantify other disturbance-induced forest dynamics, to benchmark ecological process models, and to provide critical information on forest dynamics for forest management. As such we recommend extending and testing our approach to other ecosystems in order to further evaluate the efficacy of our proposed method for quantifying forest recovery rate as a function of disturbance extent.

Acknowledgement

This work was supported by the United States Department of Energy contract No. DE-SC0012704 to Brookhaven National Laboratory. We thank the following data providers. DigitalGlobe data were provided by NASA's NGA Commercial Archive Data (cad4nasa.gsfc.nasa.gov) under the National Geospatial Intelligence Agency's NextView license agreement. Post-fire aerial color ortho-photos were provided by New York Statewide Digital Ortho-imagery Program.

Appendix A. Supplementary data

Supplementary data to this article can be found online at <https://doi.org/10.1016/j.rse.2018.03.019>.

References

- Alonzo, M., Bookhagen, B., Roberts, D.A., 2014. Urban tree species mapping using hyperspectral and lidar data fusion. *Remote Sens. Environ.* 148, 70–83.
- Alonzo, M., Morton, D.C., Cook, B.D., Andersen, H.-E., Babcock, C., Pattison, R., 2017. Patterns of canopy and surface layer consumption in a boreal forest fire from repeat airborne lidar. *Environ. Res. Lett.* 12, 10.
- Amiro, B.D., MacPherson, J.L., Desjardins, R.L., Chen, J.M., Liu, J., 2003. Post-fire carbon dioxide fluxes in the western Canadian boreal forest: evidence from towers, aircraft and remote sensing. *Agric. For. Meteorol.* 115, 91–107.
- Asner, G.P., Martin, R.E., Knapp, D.E., Tupayachi, R., Anderson, C.B., Sinca, F., Vaughn, N.R., Llactayo, W., 2017. Airborne laser-guided imaging spectroscopy to map forest trait diversity and guide conservation. *Science* 355, 385–388.
- Balch, J.K., Nepstad, D.C., Curran, L.M., Brando, P.M., Portela, O., Guilherme, P., Reuning-Scherer, J.D., de Carvalho, O., 2011. Size, species, and fire behavior predict tree and liana mortality from experimental burns in the Brazilian Amazon. *For. Ecol. Manag.* 261, 68–77.
- Barbero, R., Abatzoglou, J., Larkin, N., Kolden, C., Stocks, B., 2015. Climate change presents increasing potential for very large fires in the contiguous United States. *Int. J. Wildland Fire* 24, 892–899.
- Bartels, S.F., Chen, H.Y.H., Wulder, M.A., White, J.C., 2016. Trends in post-disturbance recovery rates of Canada's forests following wildfire and harvest. *For. Ecol. Manag.* 361, 194–207.
- Bastos, A., Gouveia, C.M., DaCamara, C.C., Trigo, R.M., 2011. Modelling post-fire vegetation recovery in Portugal. *Biogeosciences* 8, 3593–3607.
- Bolton, D.K., Coops, N.C., Wulder, M.A., 2015. Characterizing residual structure and forest recovery following high-severity fire in the western boreal of Canada using Landsat time-series and airborne lidar data. *Remote Sens. Environ.* 163, 48–60.
- Bolton, D.K., Coops, N.C., Hermosilla, T., Wulder, M.A., White, J.C., 2017. Assessing variability in post-fire forest structure along gradients of productivity in the Canadian boreal using multi-source remote sensing. *J. Biogeogr.* 44.
- Bond, W.J., Keeley, J.E., 2005. Fire as a global 'herbivore': the ecology and evolution of flammable ecosystems. *Trends Ecol. Evol.* 20, 387–394.
- Bowman, D.M.J.S., Balch, J.K., Artaxo, P., Bond, W.J., Carlson, J.M., Cochrane, M.A., D'Antonio, C.M., DeFries, R.S., Doyle, J.C., Harrison, S.P., Johnston, F.H., Keeley, J.E., Krawchuk, M.A., Kull, C.A., Marston, J.B., Moritz, M.A., Prentice, I.C., Roos, C.I., Scott, A.C., Swetnam, T.W., Van Der Werf, G.R., Pyne, S.J., 2009. Fire in the earth system. *Science* 324, 481–484.
- Brando, P.M., Nepstad, D.C., Balch, J.K., Bolker, B., Christman, M.C., Coe, M., Putz, F.E., 2012. Fire-induced tree mortality in a neotropical forest: the roles of bark traits, tree size, wood density and fire behavior. *Glob. Chang. Biol.* 18, 630–641.
- Breiman, L., 2001. Random forests. *Mach. Learn.* 45, 5–32.
- Canty, M.J., Nielsen, A.A., 2008. Automatic radiometric normalization of multitemporal satellite imagery with the iteratively re-weighted MAD transformation. *Remote Sens. Environ.* 112, 1025–1036.
- Castro, J., Allen, C.D., Molina-Morales, M., Marañón-Jiménez, S., Sánchez-Miranda, Á., Zamora, R., 2011. Salvage logging versus the use of burnt wood as a nurse object to promote post-fire tree seedling establishment. *Restor. Ecol.* 19, 537–544.
- Caughlin, T.T., Graves, S.J., Asner, G.P., Breugel, M., Hall, J.S., Martin, R.E., Ashton, M.S., Bohlman, S.A., 2016. A hyperspectral image can predict tropical tree growth rates in single-species stands. *Ecol. Appl.* 26, 2367–2373.
- Chen, X., Vogelmann, J.E., Rollins, M., Ohlen, D., Key, C.H., Yang, L., Huang, C., Shi, H., 2011. Detecting post-fire burn severity and vegetation recovery using multitemporal remote sensing spectral indices and field-collected composite burn index data in a ponderosa pine forest. *Int. J. Remote Sens.* 32, 7905–7927.

- Clark, M.L., Roberts, D.A., Clark, D.B., 2005. Hyperspectral discrimination of tropical rain forest tree species at leaf to crown scales. *Remote Sens. Environ.* 96, 375–398.
- Cook, B.D., Nelson, R.F., Middleton, E.M., Morton, D.C., McCorkel, J.T., Masek, J.G., Ranson, K.J., Ly, V., Montesano, P.M., 2013. NASA Goddard's lidar, hyperspectral and thermal (G-LiHT) airborne imager. *Remote Sens.* 5, 4045–4066.
- Dale, V.H., Joyce, L.A., McNulty, S., Neilson, R.P., Ayres, M.P., Flannigan, M.D., Hanson, P.J., Irland, L.C., Lugo, A.E., Peterson, C.J., Simberloff, D., Swanson, F.J., Stocks, B.J., Wotton, B.M., 2001. Climate change and forest disturbances. *Bioscience* 51, 723–734.
- Dash, J., Curran, P.J., 2007. Evaluation of the MERIS terrestrial chlorophyll index (MTCI). *Adv. Space Res.* 39, 100–104.
- Daughtry, C.S.T., Walthall, C.L., Kim, M.S., De Colstoun, E.B., McMurtrey, J.E., 2000. Estimating corn leaf chlorophyll concentration from leaf and canopy reflectance. *Remote Sens. Environ.* 74, 229–239.
- De Santis, A., Chuvieco, E., 2009. GeoCBI: a modified version of the composite burn index for the initial assessment of the short-term burn severity from remotely sensed data. *Remote Sens. Environ.* 113, 554–562.
- Epting, J., Verbyla, D., 2005. Landscape-level interactions of prefire vegetation, burn severity, and postfire vegetation over a 16-year period in interior Alaska. *Can. J. For. Res.* 35, 1367–1377.
- Fassnacht, F.E., Latifi, H., Sterenczak, K., Modzelewska, A., Lefsky, M., Waser, L.T., Straub, C., Ghosh, A., 2016. Review of studies on tree species classification from remotely sensed data. *Remote Sens. Environ.* 186, 64–87.
- Fernandez-Manso, A., Quintano, C., Roberts, D.A., 2016. Burn severity influence on post-fire vegetation cover resilience from Landsat MESMA fraction images time series in Mediterranean forest ecosystems. *Remote Sens. Environ.* 184, 112–123.
- Fisher, R., Muszala, S., Versteinstein, M., Lawrence, P., Xu, C., McDowell, N., Knox, R., Koven, C., Holm, J., Rogers, B., 2015. Taking off the training wheels: the properties of a dynamic vegetation model without climate envelopes, CLM4. 5 (ED). *Geosci. Model Dev.* 8, 3593–3619.
- Fisher, R.A., Koven, C.D., Anderregg, W.R.L., Christoffersen, B.O., Dietze, M.C., Farrior, C.E., Holm, J.A., Hurr, G.C., Knox, R.G., Lawrence, P.J., 2017. Vegetation demographics in Earth System Models: A review of progress and priorities. *Glob. Chang. Biol.* 24, 35–54.
- Franklin, J., Spears-Lebrun, L.A., Deutschman, D.H., Marsden, K., 2006. Impact of a high-intensity fire on mixed evergreen and mixed conifer forests in the Peninsular Ranges of southern California, USA. *For. Ecol. Manag.* 235, 18–29.
- Gamon, J.A., Penuelas, J., Field, C.B., 1992. A narrow-waveband spectral index that tracks diurnal changes in photosynthetic efficiency. *Remote Sens. Environ.* 41, 35–44.
- García, M., Riaño, D., Chuvieco, E., Salas, J., Danson, F.M., 2011. Multispectral and LiDAR data fusion for fuel type mapping using Support Vector Machine and decision rules. *Remote Sens. Environ.* 115, 1369–1379.
- Gitelson, A.A., Zur, Y., Chivkunova, O.B., Merzlyak, M.N., 2002. Assessing carotenoid content in plant leaves with reflectance spectroscopy. *Photochem. Photobiol.* 75, 272–281.
- Goetz, S.J., Fiske, G.J., Bunn, A.G., 2006. Using satellite time-series data sets to analyze fire disturbance and forest recovery across Canada. *Remote Sens. Environ.* 101, 352–365.
- Gu, H., Williams, C.A., Ghimire, B., Zhao, F., Huang, C., 2016. High-resolution mapping of time since disturbance and forest carbon flux from remote sensing and inventory data to assess harvest, fire, and beetle disturbance legacies in the Pacific Northwest. *Biogeosciences* 13, 6321.
- Hantson, S., Arneith, A., Harrison, S.P., Kelley, D.I., Prentice, I.C., Rabin, S.S., Archibald, S., Mouillot, F., Arnold, S.R., Artaxo, P., 2016. The status and challenge of global fire modelling. *Biogeosciences* 13, 3359–3375.
- Harsanyi, J.C., Chang, C.I., 1994. Hyperspectral image classification and dimensionality reduction: an orthogonal subspace projection approach. *IEEE Trans. Geosci. Remote Sens.* 32, 779–785.
- Harvey, B.J., Donato, D.C., Turner, M.G., 2014. Recent mountain pine beetle outbreaks, wildfire severity, and postfire tree regeneration in the US Northern Rockies. In: *Proceedings of the National Academy of Sciences of the United States of America*. 111. pp. 15120–15125.
- Hicke, J.A., Asner, G.P., Kasichke, E.S., French, N.H.F., Randerson, J.T., Collatz, G.J., Stocks, B.J., Tucker, C.J., Los, S.O., Field, C.B., 2003. Postfire response of North American boreal forest net primary productivity analyzed with satellite observations. *Glob. Chang. Biol.* 9, 1145–1157.
- Hochberg, E.J., Atkinson, M.J., 2003. Capabilities of remote sensors to classify coral, algae, and sand as pure and mixed spectra. *Remote Sens. Environ.* 85, 174–189.
- Holden, Z.A., Morgan, P., Smith, A.M., Vierling, L., 2010. Beyond Landsat: a comparison of four satellite sensors for detecting burn severity in ponderosa pine forests of the Gila Wilderness, NM, USA. *Int. J. Wildland Fire* 19, 449–458.
- Hoogesteger, J., Karlsson, P.S., 1992. Effects of defoliation on radial stem growth and photosynthesis in the mountain birch (*Betula pubescens* ssp. *tortuosa*). *Funct. Ecol.* 6, 317–323.
- Huang, W.L., Sun, G.Q., Dubayah, R., Cook, B., Montesano, P., Ni, W.J., Zhang, Z.Y., 2013. Mapping biomass change after forest disturbance: applying LiDAR footprint-derived models at key map scales. *Remote Sens. Environ.* 134, 319–332.
- Jin, Y.F., Randerson, J.T., Goetz, S.J., Beck, P.S.A., Lorant, M.M., Goulden, M.L., 2012. The influence of burn severity on postfire vegetation recovery and albedo change during early succession in North American boreal forests. *J. Geophys. Res. Biogeosci.* 117, 15.
- Johnstone, J.F., Rupp, T.S., Olson, M., Verbyla, D., 2011. Modeling impacts of fire severity on successional trajectories and future fire behavior in Alaskan boreal forests. *Landsc. Ecol.* 26, 487–500.
- Jordan, M.J., Patterson, W.A., Windisch, A.G., 2003. Conceptual ecological models for the Long Island pitch pine barrens: implications for managing rare plant communities. *For. Ecol. Manag.* 185, 151–168.
- Keeley, J.E., Pausas, J.G., Rundel, P.W., Bond, W.J., Bradstock, R.A., 2011. Fire as an evolutionary pressure shaping plant traits. *Trends Plant Sci.* 16, 406–411.
- Kolden, C.A., Lutz, J.A., Key, C.H., Kane, J.T., van Wageningen, J.W., 2012. Mapped versus actual burned area within wildfire perimeters: characterizing the unburned. *For. Ecol. Manag.* 286, 38–47.
- Kotliar, N.B., Hejl, S.J., Hutto, R.L., Saab, V.A., Melcher, C.P., McFadden, M.E., 2002. Effects of Fire and Post-Fire Salvage Logging on Avian Communities in Conifer-Dominated Forests of the Western United States.
- Kurczewski, F.E., Boyle, H.F., 2000. Historical changes in the pine barrens of central Suffolk County, New York. *Northeast. Nat.* 7, 95–112.
- Kurz, W.A., Stinson, G., Rampley, G.J., Dymond, C.C., Neilson, E.T., 2008. Risk of natural disturbances makes future contribution of Canada's forests to the global carbon cycle highly uncertain. *Proc. Natl. Acad. Sci.* 105, 1551–1555.
- Lasslop, G., Thonicke, K., Kloster, S., 2014. SPITFIRE within the MPI Earth system model: model development and evaluation. *J. Adv. Model. Earth Syst.* 6, 740–755.
- Lee, R.J., Chow, T.E., 2015. Post-wildfire assessment of vegetation regeneration in Bastrop, Texas, using Landsat imagery. *GIScience Remote Sens.* 1–18.
- Lentile, L.B., Holden, Z.A., Smith, A.M.S., Falkowski, M.J., Hudak, A.T., Morgan, P., Lewis, S.A., Gessler, P.E., Benson, N.C., 2006. Remote sensing techniques to assess active fire characteristics and post-fire effects. *Int. J. Wildland Fire* 15, 319–345.
- Levesque, M., Saurer, M., Siegwolf, R., Eilmann, B., Brang, P., Bugmann, H., Rigling, A., 2013. Drought response of five conifer species under contrasting water availability suggests high vulnerability of Norway spruce and European larch. *Glob. Chang. Biol.* 19, 3184–3199.
- Lewis, S.A., Wu, J.Q., Robichaud, P.R., 2006. Assessing burn severity and comparing soil water repellency, Hayman Fire, Colorado. *Hydrol. Process.* 20, 1–16.
- Liaw, A., Wiener, M., 2002. Classification and regression by randomForest. *R News* 2, 18–22.
- Little, S., 1998. Fire and plant succession in the New Jersey Pine Barrens. In: RTT, Forman (Ed.), *Pine Barrens: Ecosystem and Landscape*, pp. 297–314.
- Little, S., Moore, E.B., 1949. The ecological role of prescribed burns in the pine-oak forests of southern New Jersey. *Ecology* 30, 223–233.
- Liu, N., Budkewitsch, P., Treitz, P., 2017. Examining spectral reflectance features related to Arctic permafrost vegetation cover: implications for hyperspectral remote sensing of Arctic tundra. *Remote Sens. Environ.* 192, 58–72.
- Lloret, F., Siscart, D., Dalmases, C., 2004. Canopy recovery after drought dieback in holm-oak Mediterranean forests of Catalonia (NE Spain). *Glob. Chang. Biol.* 10, 2092–2099.
- Mantgem, P.J., Stephenson, N.L., Keeley, J.E., 2006. Forest reproduction along a climatic gradient in the Sierra Nevada, California. *For. Ecol. Manag.* 225, 391–399.
- Martin-Alcon, S., Coll, L., De Caceres, M., Guitart, L., Cabre, M., Just, A., Gonzalez-Olabarria, J.R., 2015. Combining aerial LiDAR and multispectral imagery to assess postfire regeneration types in a Mediterranean forest. *Can. J. For.* 45, 856–866.
- Marvin, D.C., Asner, G.P., Schnitzer, S.A., 2016. Liana canopy cover mapped throughout a tropical forest with high-fidelity imaging spectroscopy. *Remote Sens. Environ.* 176, 98–106.
- Mayor, A.G., Bautista, S., Llovet, J., Bellot, J., 2007. Post-fire hydrological and erosional responses of a Mediterranean landscape: seven years of catchment-scale dynamics. *Catena* 71, 68–75.
- McCarley, T.R., Kolden, C.A., Vaillant, N.M., Hudak, A.T., Smith, A.M., Wing, B.M., Kellogg, B.S., Kreitler, J., 2017. Multi-temporal LiDAR and Landsat quantification of fire-induced changes to forest structure. *Remote Sens. Environ.* 191, 419–432.
- Meng, R., Dennison, P.E., 2015. Spectroscopic analysis of green, desiccated and dead tamarisk canopies. *Photogramm. Eng. Remote. Sens.* 81, 199–207.
- Meng, R., Dennison, P., Jamison, L., van Riper, C., Nager, P., Hultine, K., Bean, D., Dudley, T., 2012. Detection of tamarisk defoliation by the Northern Tamarisk Beetle based on multitemporal Landsat 5 Thematic Mapper imagery. *GIScience Remote Sens.* 49, 510–537.
- Meng, R., Dennison, P.E., Huang, C., Moritz, M.A., D'Antonio, C., 2015. Effects of fire severity and post-fire climate on short-term vegetation recovery of mixed-conifer and red fir forests in the Sierra Nevada Mountains of California. *Remote Sens. Environ.* 171, 311–325.
- Meng, R., Wu, J., Schwager, K.L., Zhao, F., Dennison, P.E., Cook, B.D., Brewster, K., Green, T.M., Serbin, S.P., 2017. Using high spatial resolution satellite imagery to map forest burn severity across spatial scales in a Pine Barrens ecosystem. *Remote Sens. Environ.* 191, 95–109.
- Miller, J.D., Thode, A.E., 2007. Quantifying burn severity in a heterogeneous landscape with a relative version of the delta Normalized Burn Ratio (dNBR). *Remote Sens. Environ.* 109, 66–80.
- Mitri, G.H., Gitas, I.Z., 2008. Mapping the severity of fire using object-based classification of IKONOS imagery. *Int. J. Wildland Fire* 17, 431–442.
- Morgan, P., Keane, R.E., Dillon, G.K., Jain, T.B., Hudak, A.T., Karau, E.C., Sikkink, P.G., Holden, Z.A., Strand, E.K., 2014. Challenges of assessing fire and burn severity using field measures, remote sensing and modelling. *Int. J. Wildland Fire* 23, 1045–1060.
- Motzkin, G., Patterson, W.A., Foster, D.R., 1999. A historical perspective on pitch pine-scrub oak communities in the Connecticut Valley of Massachusetts. *Ecosystems* 2, 255–273.
- Myneni, R.B., Nemani, R.R., Running, S.W., 1997. Estimation of global leaf area index and absorbed par using radiative transfer models. *IEEE Trans. Geosci. Remote Sens.* 35, 1380–1393.
- Naidoo, L., Cho, M., Mathieu, R., Asner, G., 2012. Classification of savanna tree species, in the Greater Kruger National Park region, by integrating hyperspectral and LiDAR data in a Random Forest data mining environment. *ISPRS J. Photogramm. Remote Sens.* 69, 167–179.
- Nelson, K.N., Turner, M.G., Romme, W.H., Tinker, D.B., 2016. Landscape variation in tree

- regeneration and snag fall drive fuel loads in 24-year old post-fire lodgepole pine forests. *Ecol. Appl.* 26, 2422–2436.
- Pal, M., 2005. Random forest classifier for remote sensing classification. *Int. J. Remote Sens.* 26, 217–222.
- Papaik, M.J., Canham, C.D., 2006. Species resistance and community response to wind disturbance regimes in northern temperate forests. *J. Ecol.* 94, 1011–1026.
- Pausas, J.G., Keeley, J.E., 2014. Evolutionary ecology of resprouting and seeding in fire-prone ecosystems. *New Phytol.* 204, 55–65.
- Pausas, J.G., Keeley, J.E., 2017. Epicormic resprouting in fire-prone ecosystems. *Trends Plant Sci.* 204, 55–65.
- Pausas, J.G., Pratt, R.B., Keeley, J.E., Jacobsen, A.L., Ramirez, A.R., Vilagrosa, A., Paula, S., Kaneakua-Pia, I.N., Davis, S.D., 2016. Towards understanding resprouting at the global scale. *New Phytol.* 209, 945–954.
- Piao, S.L., Fang, J.Y., Ciais, P., Peylin, P., Huang, Y., Sitch, S., Wang, T., 2009. The carbon balance of terrestrial ecosystems in China. *Nature* 458, 1009–U1082.
- Qi, J., Chehbouni, A., Huete, A., Kerr, Y., Sorooshian, S., 1994. A modified soil adjusted vegetation index. *Remote Sens. Environ.* 48, 119–126.
- Quintano, C., Fernández-Manso, A., Roberts, D.A., 2013. Multiple Endmember Spectral Mixture Analysis (MESMA) to map burn severity levels from Landsat images in Mediterranean countries. *Remote Sens. Environ.* 136, 76–88.
- Reich, P.B., Abrams, M.D., Ellsworth, D.S., Kruger, E.L., Tabone, T.J., 1990. Fire affects ecophysiology and community dynamics of central Wisconsin oak forest regeneration. *Ecology* 71, 2179–2190.
- Rich, R.L., Frelich, L.E., Reich, P.B., 2007. Wind-throw mortality in the southern boreal forest: effects of species, diameter and stand age. *J. Ecol.* 95, 1261–1273.
- Roberts, D.A., Gardner, M., Church, R., Ustin, S., Scheer, G., Green, R.O., 1998. Mapping chaparral in the Santa Monica Mountains using multiple endmember spectral mixture models. *Remote Sens. Environ.* 65, 267–279.
- Rogers, B.M., Soja, A.J., Goulden, M.L., Randerson, J.T., 2015. Influence of tree species on continental differences in boreal fires and climate feedbacks. *Nat. Geosci.* 8, 228–234.
- Roujean, J.-L., Breon, F.-M., 1995. Estimating PAR absorbed by vegetation from bidirectional reflectance measurements. *Remote Sens. Environ.* 51, 375–384.
- Schwalm, C.R., Anderegg, W.R.L., Michalak, A.M., Fisher, J.B., Biondi, F., Koch, G., Litvak, M., Ogle, K., Shaw, J.D., Wolf, A., 2017. Global patterns of drought recovery. *Nature* 548, 202–205.
- Seidl, R., Fernandes, P.M., Fonseca, T.F., Gillet, F., Jönsson, A.M., Merganicová, K., Netherer, S., Arpacı, A., Bontemps, J.-D., Bugmann, H., González-Olabarria, J.R., Lasch, P., Meredieu, C., Moreira, F., Schelhaas, M.-J., Mohren, F., 2011. Modelling natural disturbances in forest ecosystems: a review. 222, 903–924.
- Serbin, S.P., Ahl, D.E., Gower, S.T., 2013. Spatial and temporal validation of the MODIS LAI and FPAR products across a boreal forest wildfire chronosequence. *Remote Sens. Environ.* 133, 71–84.
- Sharpe, M., Hwang, H., Schroeder, D., Ryu, S.R., Lieffers, V.J., 2017. Prescribed fire as a tool to regenerate live and dead serotinous jack pine (*Pinus banksiana*) stands. *Int. J. Wildland Fire* 26, 478–484.
- Shendryk, I., Broich, M., Tulbure, M.G., McGrath, A., Keith, D., Alexandrov, S.V., 2016. Mapping individual tree health using full-waveform airborne laser scans and imaging spectroscopy: a case study for a floodplain eucalypt forest. *Remote Sens. Environ.* 187, 202–217.
- Smith, A.M., Sparks, A.M., Kolden, C.A., Abatzoglou, J.T., Talhelm, A.F., Johnson, D.M., Boschetti, L., Lutz, J.A., Apostol, K.G., Yedinak, K.M., 2016. Towards a new paradigm in fire severity research using dose–response experiments. *Int. J. Wildland Fire* 25, 158–166.
- Sparks, A.M., Kolden, C.A., Talhelm, A.F., Smith, A.M.S., Apostol, K.G., Johnson, D.M., Boschetti, L., 2016. Spectral indices accurately quantify changes in seedling physiology following fire: towards mechanistic assessments of post-fire carbon cycling. *Remote Sens.* 8.
- Stavros, E.N., Tane, Z., Kane, V.R., Veraverbeke, S., McGaughey, R.J., Lutz, J.A., Ramirez, C., Schimel, D., 2016. Unprecedented remote sensing data over King and Rim megafires in the Sierra Nevada Mountains of California. *Ecology* 97, 3244.
- Storey, E.A., Stow, D.A., O’Leary, J.F., 2016. Assessing postfire recovery of chamise chaparral using multi-temporal spectral vegetation index trajectories derived from Landsat imagery. *Remote Sens. Environ.* 183, 53–64.
- Swanson, M.E., Franklin, J.F., Beschta, R.L., Crisafulli, C.M., DellaSala, D.A., Hutto, R.L., Lindenmayer, D.B., Swanson, F.J., 2011. The forgotten stage of forest succession: early-successional ecosystems on forest sites. *Front. Ecol. Environ.* 9, 117–125.
- Tang, H., Dubayah, R., 2017. Light-driven growth in Amazon evergreen forests explained by seasonal variations of vertical canopy structure. *Proc. Natl. Acad. Sci.* 201616943.
- Torabzadeh, H., Morsdorf, F., Schaepman, M.E., 2014. Fusion of imaging spectroscopy and airborne laser scanning data for characterization of forest ecosystems—a review. *ISPRS J. Photogramm. Remote Sens.* 97, 25–35.
- Torresan, C., Berton, A., Carotenuto, F., Di Gennaro, S.F., Gioli, B., Matese, A., Miglietta, F., Vagnoli, C., Zaldei, A., Wallace, L., 2017. Forestry applications of UAVs in Europe: a review. *Int. J. Remote Sens.* 38, 2427–2447.
- Tucker, C.J., 1979. Red and photographic infrared linear combinations for monitoring vegetation. *Remote Sens. Environ.* 8, 127–150.
- Turner, M.G., 2010. Disturbance and landscape dynamics in a changing world. *Ecology* 91, 2833–2849.
- Turner, M.G., Romme, W.H., Gardner, R.H., Hargrove, W.W., 1997. Effects of fire size and pattern on early succession in Yellowstone National Park. *Ecol. Monogr.* 67, 411–433.
- Turner, M.G., Baker, W.L., Peterson, C.J., Peet, R.K., 1998. Factors influencing succession: lessons from large, infrequent natural disturbances. *Ecosystems* 1, 511–523.
- Turner, M.G., Whitby, T.G., Tinker, D.B., Romme, W.H., 2016. Twenty-four years after the Yellowstone Fires: are postfire lodgepole pine stands converging in structure and function? *Ecology* 97, 1260–1273.
- van der Werf, G.R., Morton, D.C., DeFries, R.S., Olivier, J.G., Kasibhatla, P.S., Jackson, R.B., Collatz, G.J., Randerson, J., 2009. CO₂ emissions from forest loss. *Nat. Geosci.* 2, 737–738.
- van der Werf, G.R., Randerson, J.T., Giglio, L., Collatz, G.J., Mu, M., Kasibhatla, P.S., Morton, D.C., DeFries, R.S., Jin, Y., van Leeuwen, T.T., 2010. Global fire emissions and the contribution of deforestation, savanna, forest, agricultural, and peat fires (1997–2009). *Atmos. Chem. Phys.* 10, 11707–11735.
- Veraverbeke, S., Hook, S., Hulley, G., 2012. An alternative spectral index for rapid fire severity assessments. *Remote Sens. Environ.* 123, 72–80.
- Vogelmann, J.E., Rock, B.N., Moss, D.M., 1993. Red edge spectral measurements from sugar maple leaves. *Int. J. Remote Sens.* 14, 1563–1575.
- Westerling, A.L., Hidalgo, H.G., Cayan, D.R., Swetnam, T.W., 2006. Warming and earlier spring increase Western U.S. forest wildfire activity. *Science* 313, 940–943.
- White, J.D., Ryan, K.C., Key, C.C., Running, S.W., 1996. Remote sensing of forest fire severity and vegetation recovery. *Int. J. Wildland Fire* 6, 125–136.
- Whittaker, R.H., Woodwell, G.M., 1969. Structure, production and diversity of the oak-pine Forest at Brookhaven, New York. *J. Ecol.* 57, 155–174.
- Wilson, A.M., Latimer, A.M., Silander, J.A., 2015. Climatic controls on ecosystem resilience: Postfire regeneration in the Cape Floristic Region of South Africa. In: *Proceedings of the National Academy of Sciences of the United States of America*. vol. 112. pp. 9058–9063.
- Yang, J., Tian, H., Tao, B., Ren, W., Pan, S., Liu, Y., Wang, Y., 2015. A growing importance of large fires in conterminous United States during 1984–2012. *J. Geophys. Res. Biogeosci.* 120, 2625–2640.
- Yang, J., Pan, S., Dangal, S., Zhang, B., Wang, S., Tian, H., 2017. Continental-scale quantification of post-fire vegetation greenness recovery in temperate and boreal North America. *Remote Sens. Environ.* 199, 277–290.
- Yu, X., Hyyppä, J., Vastaranta, M., Holopainen, M., Viitala, R., 2011. Predicting individual tree attributes from airborne laser point clouds based on the random forests technique. *ISPRS J. Photogramm. Remote Sens.* 66, 28–37.
- Zarco-Tejada, P.J., Miller, J.R., Mohammed, G.H., Noland, T.L., Sampson, P.H., 2001. Estimation of chlorophyll fluorescence under natural illumination from hyperspectral data. *Int. J. Appl. Earth Obs. Geoinf.* 3, 321–327.
- Zarco-Tejada, P.J., Berjón, A., López-Lozano, R., Miller, J.R., Martín, P., Cachorro, V., González, M.R., De Frutos, A., 2005. Assessing vineyard condition with hyperspectral indices: leaf and canopy reflectance simulation in a row-structured discontinuous canopy. *Remote Sens. Environ.* 99, 271–287.
- Zhao, F.R., Meng, R., Huang, C.Q., Zhao, M.S., Zhao, F.A., Gong, P., Yu, L., Zhu, Z.L., 2016. Long-term post-disturbance Forest recovery in the greater yellowstone ecosystem analyzed using Landsat time series stack. *Remote Sens.* 8.
- Zhao, K., Suarez, J.C., Garcia, M., Hu, T., Wang, C., Londo, A., 2018. Utility of multi-temporal lidar for forest and carbon monitoring: tree growth, biomass dynamics, and carbon flux. *Remote Sens. Environ.* 204, 883–897.
- Zweifel, R., Rigling, A., Dobbertin, M., 2009. Species-specific stomatal response of trees to drought - a link to vegetation dynamics? *J. Veg. Sci.* 20, 442–454.